

**High precision measurement of the D-line
tune-out wavelength in ^{87}Rb using a
Bose-Einstein condensate interferometer**

Robert H. Leonard

B.S., West Virginia University, 2008

A Dissertation presented to the Graduate Faculty
of the University of Virginia in Candidacy for the Degree of
Doctor of Philosophy

Department of Physics

University of Virginia

November, 2016

Contents

1	Magic Wavelength	4
1.1	Motivation	4
1.2	Theory	6
1.2.1	Semi-Classical Calculation of the Dynamic Polarizability	6
1.2.2	Tensor Polarizability	14
1.2.3	Tune-Out Wavelength	15
2	BEC Interferometer Apparatus	18
2.1	BEC Creation	18
2.1.1	Laser Cooling & Magneto-Optical Trap	18
2.1.2	Optical Pumping & Magnetic Trap	19
2.1.3	Forced RF Evaporation	22
2.1.4	Time-Orbiting Potential Trap	22
2.2	BEC Wave Guide	24
2.3	Bragg Splitting & Reflecting	25
2.4	Confinement Effects & Interferometer Symmetry	27
2.5	Absorption Imaging	30
3	Tune-Out Wavelength Experiment	32
3.1	Overview	32

3.2	Detailed Experimental Procedure	34
3.2.1	Stark Beam Alignment	35
3.2.2	Broadband Light	37
3.2.3	Wavelength Measurement	41
3.2.4	Vector Polarizability	43
3.2.5	Tensor Polarizability	49
4	Results	51
4.1	Results of The Tune-out Wavelength Measurement	51
4.2	Error Analysis	52
4.3	Comparison to Theory	56
4.3.1	Uncertainty in Theoretical Tune-Out Wavelength Prediction	58
5	Outlook	62
5.1	Future Tune-out Wavelength Measurements	62
	Appendices	66
A	AOM Configuration	67
B	Reduced Electric Dipole Matrix Elements	69
C	Kinetic Imaging	71
C.1	Overview	71
C.2	Implementation	73
C.3	Image Processing	76
	Bibliography	83

List of Figures

1.1	Tune-out Wavelength for ^{87}Rb	17
2.1	Polarization Confinement in a MOT	20
2.2	Schematic of Vacuum Chamber Setup.	21
2.3	RF Evaporative Cooling.	22
2.4	Schematic of Bragg Splitting	26
2.5	Phase Shift Dependence of N_0/N	28
2.6	Confinement Induced Phase Gradients	29
2.7	Phase Gradient Canceling Trajectory	30
2.8	Schematic of Absorption Imaging	31
3.1	Phase shift Measurements at $\lambda = 790.03170$ nm and 790.03251 nm	33
3.2	Tune-out Wavelength Data	34
3.3	Atom-wave Trajectories During Polarizability Measurements	35
3.4	Schematic of Atom & Stark Beam Imaging	36
3.5	Scattering Rates With And Without Band-Pass Filter.	39
3.6	Schematic of Spectral Filtering Optics	42
3.7	Orientation of the rotating bias field in the experimental apparatus.	45
3.8	Vector Polarizability Time Average	46
3.9	Stark Beam Pulse Timing During Polarization Measurement	48

4.1	Polarization dependence of tune-out wavelength.	52
5.1	420 nm Tune-out Wavelengths in ^{87}Rb	63
A.1	Saturated Absorption AOM Configuration	67
A.2	Tune-out Wavelength AOM Configuration	68
C.1	Comparison of kinetic and normal images.	72
C.2	Schematic of kinetic imaging process.	73
C.3	Imaging Probe Pulse & Logic Output Timing For Kinetic Imaging Mode . .	75

List of Tables

3.1	Saturation Absorption Measurements	42
4.1	Error Budget	56
4.2	Polarizability contributions at tune-out wavelength	59
4.3	Theoretical Tune-out dependence on $5P$ dipole values.	61
B.1	Dipole Matrix Elements for D_1 Line	70
B.2	Dipole Matrix Elements for D_2 Line	70

Abstract

An atom-wave interferometer using a Bose-Einstein condensate of ^{87}Rb in the $F = 2$ hyperfine ground state was used to measure the wavelength of light at which the scalar dynamic electric polarizability equals zero. Vector contributions to the polarizability are minimized through the use of linearly polarized light. The polarization of the light is measured at the atoms using the same atom-wave interferometer. A rotating magnetic field further reduces the vector polarizability through temporal averaging. Tensor contributions to the polarizability are measured, and removed from the value reported here. The wavelength is measured using a wavemeter which was calibrated using known saturation absorption lines in K, Rb, and Cs. The tune-out wavelength between the $5S$ ground state and $5P$ excited states was found to be $790.032326(32)$ nm. This measurement marks a 50-fold improvement over previous tune-out wavelength measurements. The measured tune-out wavelength is used to determine the ratio of matrix elements $|\langle 5P_{3/2} || d || 5S \rangle| / |\langle 5P_{1/2} || d || 5S \rangle| = 1.99217(3)$, a 100-fold improvement over previous experimental values. A theoretical determination of the tune-out wavelength is found to be consistent with the experiment, with uncertainty estimates for the theory about an order of magnitude larger than the experimental precision.

Acknowledgments

Nothing in this thesis would have been possible without the guidance of my advisor, Cass Sackett. Cass proposed the research outlined in this thesis and shouldered the immense responsibility of running the lab. Cass is easily one of the best teachers I've known. He mentored me when I first began working in the lab, and worked with me to solve many issues with the experiment. Despite my many setbacks, he has always remained supportive and optimistic.

I would also like to thank John Burke, Jeremy Hughes, and Vanessa Leung who patiently mentored me when I first joined Casslab. I knew nothing about experimental physics when I first joined. Each of you taught me more than I will ever realize.

I also want to thank, Robert Horne, who was both a college and a friend. Rob and I joined the lab at the same time, and worked together on our first project (building a lock circuit for one of the most unstable laser in the world). We shared many early struggles, both in the lab and in the classroom. Our discussions both challenged and depend my understanding of physics, while our irreverent conversations helped keep me sane.

I would especially like to thank Adam Fallon, who joined the lab during my last year at UVA. Adam is one of the brightest people Ive ever had the opportunity to work with. And while I began my work with Adam as a mentor, Adam quickly became my peer. Adam helped diagnose and solve many issues with the tune-out wavelength measurement. When we finally started making measurements, Adam arrived early in the morning (a.k.a. before 11 am). He warmed-up the lasers, optimized the Bragg splitting, and started the

frustrating process of aligning the Stark beam. I genuinely don't know how I would have completed these measurements without Adams help.

I would also like to thank many of my teachers. My high school math teachers, Ms. Dillinger and Mrs. Goode, who helped to create a strong foundation to build upon. As well as Dr. Enrique Moreno, a master teacher who taught many of the classes I took at WVU. And especially my undergraduate research advisor, Dr. Martina E. Bachlechner, who nurtured and guided my interest in physics.

Lastly I would like to thank my parents. No matter what happened, I always knew I would have your love and support. It was the comfort I felt in knowing this that helped me through my most difficult times: when everything seemed to break, nothing seemed to work, and progress was elusive. Even when I felt like I had lost everything that I had been working towards, I knew that hadn't lost your love and support.

Chapter 1

Magic Wavelength

1.1 Motivation

When an external electric field is applied to an atom, the charge distribution of the atom is disturbed. The atom's response to an applied electric field is described by the polarizability. Polarizability plays an important role in a variety of physical phenomena including light scattering[1], light trapping[2, 3], van der Waals interactions[4], and the Casimir-Polder effect[5]. Moreover, an atom's polarizability is determined by various elements of the dipole matrix of the atomic waveform. These matrix elements are also needed to interpret important measurements such as parity nonconservation. These measurements provide an important tool used to probe for the existence of new physics beyond the standard electroweak model [6, 7, 8].

Polarizability is of practical importance in the development of more precise atomic clocks. Atomic clocks require precise knowledge of the optical transition frequencies. Shifts due to atom interactions with environmental blackbody radiation are one of the largest sources of uncertainty in optical transition frequencies. Because it is impossible to eliminate the blackbody radiation emitted by an experimental apparatus, these shifts are unavoidable and must be corrected using theoretical calculations. At present, these

theoretical calculations are limited by the uncertainty in the dynamic polarizability [9, 10, 11, 12].

Previous measurements of the dynamic polarizability have been limited to an uncertainty of around 1%. These measurements are limited by the inability to precisely measure the intensity of the applied field [13, 14]. With this limitation in mind, we seek a polarizability measurement which is independent of the intensity of the applied field. Towards this end, we seek to measure a wavelength where the dynamic dipole polarizability is zero, $\alpha(\omega) = 0$. The wavelengths where this occur are known as tune-out wavelengths [15] or magic-zero wavelengths and will be denoted as λ_0 . As I will show in Section 1.2.3, the tune-out wavelength will be independent of the intensity of the applied field for the intensities used in this measurement.

A precision measurement of λ_0 provides a useful accuracy check for *ab initio* calculations of $\alpha(\omega)$, as well as an input parameter in semi-empirical calculations. As a result, a precise measurement of λ_0 will provide a tool for improving the theoretical accuracy $\alpha(\omega)$. As described above, the improved theoretical accuracy of $\alpha(\omega)$ will reduce the uncertainty in atomic clock measurements and improve the precision of theoretical models which describe physical phenomena that arise from the polarizability. Moreover, a precision measurement of λ_0 will also yield an accurate measure of the ratio of the dipole matrix elements coupling the $5S_{1/2}$ ground state to the $5P_{1/2}$ and $5P_{3/2}$ excited states. Knowledge of the dipole matrix elements is useful in the interpretation of the results of parity nonconservation measurements.

In addition to providing a tool for improving the theoretical accuracy in $\alpha(\omega)$, precise knowledge of λ_0 has a direct application in the creation of species specific optical lattices and far-off-resonance traps (FORTs) [16, 15]. FORTs rely on the induced dipole-light interaction to trap atoms. The resulting force is given by

$$\mathbf{F} = \frac{1}{2c\epsilon_0} \alpha(\omega) \nabla I(\mathbf{r}) \quad (1.1)$$

where I is the intensity of the trapping light. At the tune-out wavelength, the dipole-light force vanishes, as $\alpha = 0$. As we will see in Section 1.2, the tune-out wavelength is species specific. Thus, an optical trap tuned to the tune-out wavelength of one species, known as the spectator species, will trap other species while leaving the spectator species unaffected.

1.2 Theory

When an external electric field \mathcal{E} is applied to an atom, the charge distribution of the atom is disturbed, inducing an electric dipole \mathbf{d} . To first order $\mathbf{d} = \alpha \mathcal{E}$, where α is the dipole polarizability. The induced dipole interacts with the external electric field creating an interaction energy [1] given by

$$\Delta E = -\frac{1}{2}\alpha \mathcal{E}^2 \quad (1.2)$$

The polarizability of an atom in an alternating electric field is given by the dynamic dipole polarizability $\alpha(\omega)$. For the electric field created by a light source, we can use $I = c \epsilon \langle \mathcal{E}^2 \rangle$ to rewrite Eq. (1.2) as

$$\langle \Delta E \rangle = -\frac{1}{2c\epsilon} \alpha(\omega) I \quad (1.3)$$

The energy shift described by Eq. (1.3) is known as the ac Stark shift.

1.2.1 Semi-Classical Calculation of the Dynamic Polarizability

Following [13, 17] we will derive a formula for the dynamic polarizability of an atom. Starting with the Time-Dependent Schrödinger Equation

$$i \hbar \frac{d|\Psi\rangle}{dt} = H |\Psi\rangle \quad (1.4)$$

consider an electron in an atom exposed to off-resonant light. For an intense field, we may treat the field classically [18]. The Hamiltonian may be expressed as

$$H = H_a + V(t) \quad (1.5)$$

where H_a is the unperturbed Hamiltonian of the atom and $V(t)$ is the time-dependent perturbation arising from the dipole-field interaction. Using the dipole approximation, we may write $V(t)$ as

$$\begin{aligned} V(t) &= -\mathbf{d} \cdot \boldsymbol{\mathcal{E}} \cos(\omega_L t) \\ &= -\mathcal{E}(\mathbf{d} \cdot \hat{\boldsymbol{\epsilon}}(t)) \cos(\omega_L t) \end{aligned} \quad (1.6)$$

where $\hat{\boldsymbol{\epsilon}}$ is the polarization unit vector and ω_L is the angular frequency of the light. For the case of linearly polarized light, which we will consider here, the polarization unit vector $\hat{\boldsymbol{\epsilon}}$ does not depend on time. In this case we may rewrite Eq. (1.6) as

$$V(t) = V_+ e^{-i\omega_L t} + V_- e^{i\omega_L t} \quad (1.7)$$

where $V_+ = V_- = -(\mathbf{d} \cdot \boldsymbol{\mathcal{E}})/2$.

For linearly polarized light, the vector polarizability, which will be discussed in Section 1.2.2, vanishes. A derivation of the vector polarizability using the Floquet formalism is found in Ref. [19].

Floquet Formalism

In cases involving a periodic time-dependent Hamiltonian, we may employ the Floquet formalism to transform the problem into a set of time-independent equations. This process is similar to the Bloch theorem approach which is used to solve problems involving a spatially periodic Hamiltonian. Although the Hamiltonian in Eq. (1.5) explicitly depends

on time, it is useful to compare this to the time-independent Hamiltonian. For a time-independent Hamiltonian, the eigenstates of the Schrödinger Equation evolve in time according to

$$|\Psi_n(t, \mathbf{r})\rangle = e^{-i \frac{E_n t}{\hbar}} \psi_n(\mathbf{r}) \quad (1.8)$$

where E_n is the energy of the stationary state $|\Psi_n\rangle$. For a periodic Hamiltonian, like the one shown in Eq. (1.5), the quasienergy ϵ is defined by [20]

$$|\Psi_n(t + T, \mathbf{r})\rangle = e^{-i \frac{\epsilon_n T}{\hbar}} |\Psi_n(t, \mathbf{r})\rangle \quad (1.9)$$

where T is the period of the Hamiltonian. The quasi-energy used in the Floquet formalism is analogous to the crystal wave vector of the Bloch theorem.

Comparing Eq. (1.8) and Eq. (1.9) we see that the quasienergy ϵ_n is analogous to the energy E_n of a time-independent Hamiltonian. Factoring out the time dependence associated with the quasienergy gives

$$|\Psi_n(t, \mathbf{r})\rangle = e^{-i \frac{\epsilon_n t}{\hbar}} |u_n(t, \mathbf{r})\rangle \quad (1.10)$$

where $|u_n\rangle$ is a Floquet state which is analogous to a stationary state in a time-independent Hamiltonian. For the Hamiltonian in Eq. (1.5), the Floquet state $|u_n(t)\rangle$ has the same periodicity as the perturbation $V(t)$. Therefore we may expand $|u_n(t)\rangle$ as a Fourier Series

$$|u_n(t, \mathbf{r})\rangle = \sum_{m=-\infty}^{+\infty} e^{-i m \omega_L t} |\psi_{n,m}(\mathbf{r})\rangle \quad (1.11)$$

where $|\psi_{n,m}\rangle$ is referred to as the m -th mode of the Floquet state. Plugging Eq. (1.10)

and (1.11) into the Time-Dependent Schrödinger Equation gives

$$\begin{aligned} & \epsilon_n \sum_m e^{-im\omega_L t} |\psi_{n,m}\rangle + \sum_m m \hbar\omega_L e^{-im\omega_L t} |\psi_{n,m}\rangle \\ &= H_a \sum_m e^{-im\omega_L t} |\psi_{n,m}\rangle + V_+ \sum_m e^{-i(m+1)\omega_L t} |\psi_{n,m}\rangle + V_- \sum_m e^{-i(m-1)\omega_L t} |\psi_{n,m}\rangle \end{aligned} \quad (1.12)$$

Comparing terms with the same time dependence gives the following time-independent equation

$$(\epsilon_n + m \hbar\omega_L - H_a) |\psi_{n,m}\rangle = V_+ |\psi_{n,(m-1)}\rangle + V_- |\psi_{n,(m+1)}\rangle \quad (1.13)$$

As we can see from Eq. (1.13), the dipole interaction couples the m -th mode of the Floquet state to the $m\pm 1$ mode. The mode m can be interpreted as the number of photons involved in a process, where the V_+ term corresponds to the absorption of a photon and the V_- term corresponds to the emission of a photon [21].

Time-Independent Perturbation Theory

We proceed by applying Time-Independent Perturbation Theory to Eq. (1.13). Since Eq. (1.13) relates different Floquet modes of the same quasienergy state, I will drop the index n . We expand the quasienergy and Floquet state in a perturbation series

$$\epsilon = \epsilon^{(0)} + \epsilon^{(1)} + \epsilon^{(2)} + \dots \quad (1.14)$$

$$|\psi_m\rangle = |\psi_m^{(0)}\rangle + |\psi_m^{(1)}\rangle + |\psi_m^{(2)}\rangle + \dots \quad (1.15)$$

By definition the zeroth order results correspond to the solution of the unperturbed Hamiltonian, thus

$$\epsilon = E^{(0)} \quad (1.16)$$

$$|\psi_m\rangle = |\psi_0^{(0)}\rangle \quad (1.17)$$

where $H_a |\psi_0^{(0)}\rangle = E^{(0)} |\psi_0^{(0)}\rangle$. Note that in order to have the appropriate time dependence in the unperturbed solution, $|\psi_m^{(0)}\rangle = 0 \quad \forall m \neq 0$.

Keeping only the first order terms in Eq. (1.13) gives

$$(\epsilon^{(0)} + m \hbar \omega_L - H_a) |\psi_m^{(1)}\rangle + \epsilon^{(1)} |\psi_m^{(0)}\rangle = V_+^{(1)} |\psi_{m-1}^{(0)}\rangle + V_-^{(1)} |\psi_{m+1}^{(0)}\rangle \quad (1.18)$$

To find the first order correction to the quasienergy, we take the scalar product of above equation with $|\psi_0^{(0)}\rangle$ for $m = 0$

$$\begin{aligned} (\epsilon^{(0)} - \epsilon^{(0)}) \langle \psi_0^{(0)} | \psi_0^{(1)} \rangle + \epsilon^{(1)} \langle \psi_0^{(0)} | \psi_0^{(0)} \rangle &= 0 \\ \epsilon^{(1)} &= 0 \end{aligned} \quad (1.19)$$

To find the first order correction to Floquet modes, we plug $\epsilon^{(1)} = 0$ into Eq. (1.18) and looking for values of m which give non-zero terms on the right hand side of the equation (which only happens for $m = \pm 1$).

$$(\epsilon^{(0)} \pm \hbar \omega_L - H_a) |\psi_{\pm 1}^{(1)}\rangle = V_{\pm}^{(1)} |\psi_0^{(0)}\rangle \quad (1.20)$$

The operator $\epsilon^{(0)} \pm \hbar \omega_L - H_a$ can be inverted to solve for $|\psi_{\pm 1}^{(1)}\rangle$ giving

$$|\psi_{\pm 1}^{(1)}\rangle = G_{\pm} V_{\pm}^{(1)} |\psi_0^{(0)}\rangle \quad (1.21)$$

where G_{\pm} is the Green's function

$$G_{\pm} = (\epsilon^{(0)} \pm \hbar \omega_L - H_a)^{-1} \quad (1.22)$$

I will return to this Green's function further on this section, however, let's proceed by calculating the second-order perturbation in the quasienergy.

Keeping second order terms in Eq. (1.13) and using $\epsilon^{(1)} = 0$ gives

$$(\epsilon^{(0)} + m \hbar \omega_L - H_a) |\psi_m^{(2)}\rangle + \epsilon^{(2)} |\psi_m^{(0)}\rangle = V_+^{(1)} |\psi_{m-1}^{(1)}\rangle + V_-^{(1)} |\psi_{m+1}^{(1)}\rangle \quad (1.23)$$

To find the second order correction to the quasienergy, we take the scalar product of above equation with $|\psi_0^{(0)}\rangle$ when $m = 0$

$$\epsilon^{(2)} = \langle \psi_0^{(0)} | V_+^{(1)} | \psi_{-1}^{(1)} \rangle + \langle \psi_0^{(0)} | V_-^{(1)} | \psi_{+1}^{(1)} \rangle \quad (1.24)$$

Using Eq. (1.21), we may rewrite the equation above in terms of the Green's function G_{\pm} , and the unperturbed wave function $|\psi_0^{(0)}\rangle$.

$$\epsilon^{(2)} = \langle \psi_0^{(0)} | V_+^{(1)} G_- V_-^{(1)} | \psi_0^{(0)} \rangle + \langle \psi_0^{(0)} | V_-^{(1)} G_+ V_+^{(1)} | \psi_0^{(0)} \rangle \quad (1.25)$$

To evaluate Eq. (1.24) we need to rewrite the Green's function in a more useful form. Consider the Green's Function G_{\pm} acting on an arbitrary wave function $|\phi\rangle$ to produce a new function $|\tilde{\phi}\rangle$.

$$|\tilde{\phi}\rangle = G_{\pm} |\phi\rangle \quad (1.26)$$

$$|\tilde{\phi}\rangle = (\epsilon_i^{(0)} \pm \hbar \omega_L - H_a)^{-1} |\phi\rangle$$

$$(\epsilon_i^{(0)} \pm \hbar \omega_L - H_a) |\tilde{\phi}\rangle = |\phi\rangle$$

Using the projection operator to rewrite the equation above in terms of the eigenstates of

H_a gives

$$\begin{aligned} \sum_n |\psi_n\rangle \langle \psi_n| (\epsilon_i^{(0)} \pm \hbar\omega_L - H_a) |\tilde{\phi}\rangle &= |\phi\rangle \\ \sum_n (\epsilon_i^{(0)} \pm \hbar\omega_L - \epsilon_n^{(0)}) |\psi_n\rangle \langle \psi_n| \tilde{\phi}\rangle &= |\phi\rangle \end{aligned}$$

Taking the scalar product of the equation above with an arbitrary eigenstate of H_a , gives

$$\begin{aligned} \sum_n (\epsilon_i^{(0)} \pm \hbar\omega_L - \epsilon_n^{(0)}) \langle \psi_f | \psi_n\rangle \langle \psi_n | \tilde{\phi}\rangle &= \langle \psi_f | \phi\rangle \\ (\epsilon_i^{(0)} \pm \hbar\omega_L - \epsilon_f^{(0)}) \langle \psi_f | \tilde{\phi}\rangle &= \langle \psi_f | \phi\rangle \\ \langle \psi_f | \tilde{\phi}\rangle &= \frac{\langle \psi_f | \phi\rangle}{\epsilon_i^{(0)} \pm \hbar\omega_L - \epsilon_f^{(0)}} \end{aligned} \quad (1.27)$$

where we assumed that $\hbar\omega_L \neq \epsilon_f^{(0)} - \epsilon_i^{(0)}$. Plugging Eq. (1.27) into the identity $|\tilde{\phi}\rangle = \sum_n |\psi_n\rangle \langle \psi_n | \tilde{\phi}\rangle$ gives

$$\begin{aligned} |\tilde{\phi}\rangle &= \sum_f |\psi_f\rangle \langle \psi_f | \tilde{\phi}\rangle \\ |\tilde{\phi}\rangle &= \left(\sum_f \frac{|\psi_f\rangle \langle \psi_f|}{\epsilon_i^{(0)} \pm \hbar\omega_L - \epsilon_f^{(0)}} \right) |\phi\rangle \end{aligned} \quad (1.28)$$

Comparing Eq. (1.28) with Eq. (1.26) reveals that

$$G_{\pm} = \sum_f \frac{|\psi_f\rangle \langle \psi_f|}{\epsilon_i^{(0)} \pm \hbar\omega_L - \epsilon_f^{(0)}} \quad (1.29)$$

Plugging the Green's function into Eq. (1.24) and using $V_- = V_+ = \frac{-d \cdot \mathcal{E}}{2}$ we can finally

calculate the second-order perturbation to ϵ_i

$$\begin{aligned}\epsilon_i^{(2)} &= \sum_f |\langle \psi_0^{(0)} | V_+^{(1)} | \psi_f^{(0)} \rangle|^2 \left(\frac{1}{\epsilon_i^{(0)} - \epsilon_f^{(0)} - \hbar\omega_L} + \frac{1}{\epsilon_i^{(0)} - \epsilon_f^{(0)} + \hbar\omega_L} \right) \\ &= \frac{1}{\hbar} \sum_f |\langle \psi_0^{(0)} | \mathbf{d} | \psi_f^{(0)} \rangle|^2 \langle \mathcal{E}^2 \rangle \left(\frac{\omega_f}{\omega_f^2 - \omega_L^2} \right)\end{aligned}\quad (1.30)$$

where $\hbar\omega_f = \epsilon_i^{(0)} - \epsilon_f^{(0)}$.

Comparing Eq. (1.30) with Eq. (1.2) reveals

$$\alpha(\omega) = \frac{2}{\hbar} \sum_f |\langle \psi_0 | \mathbf{d} | \psi_f \rangle|^2 \left(\frac{\omega_f}{\omega_f^2 - \omega_L^2} \right)\quad (1.31)$$

where the sum is taken over all bound excited states as well as the continuum. For alkali atoms, the polarizability is dominated by the coupling of the valence electron to the first few excited states. As a result, it is convenient to separate the valence contributions to the polarizability

$$\alpha(\omega) = \alpha^v(\omega) + \alpha_{other}\quad (1.32)$$

where α_{other} includes contributions from core electrons as well as corrections due to the interaction between the core and valence electrons. For light that is far detuned from the resonances of the core electrons, α_{other} is approximately independent of the frequency. Using Eq. (1.31), we can rewrite the valence contribution to the polarizability $\alpha^v(\omega)$ as

$$\alpha^v(\omega) = \frac{2}{\hbar} \sum_{n', F', m'_F} |\langle n, F, m | \mathbf{d} | n', F', m'_F \rangle|^2 \left(\frac{\omega_f}{\omega_f^2 - \omega_L^2} \right)\quad (1.33)$$

where the sum in Eq. (1.33) runs over the excited states of the valence electron.

1.2.2 Tensor Polarizability

In general, the electric dipole \mathbf{d} does not point in the same direction as the externally applied field \mathcal{E} . Furthermore, the electric field is not always linearly polarized. As a result, the dipole-field interaction potential (Eq. (1.2)) must be expressed in terms of a tensor as

$$\Delta E = \sum_{i,j} \frac{1}{2} \alpha_{ij} \mathcal{E}_i \mathcal{E}_j \quad (1.34)$$

It is convenient to decompose the polarizability into an irreducible representation of spherical tensors so that the m_F and orientation dependencies are explicitly shown. When written in this way, the polarizability is given by [22, 23, 24, 25]

$$\begin{aligned} \alpha(\omega) = & \alpha^{(0)}(\omega) + \mathcal{A} \cos \theta_k \frac{m_F}{2F} \alpha^{(1)}(\omega) \\ & + \left(\frac{3 \cos^2 \phi - 1}{2} \right) \frac{3m_F^2 - F(F+1)}{2F(2F-1)} \alpha^{(2)}(\omega) \end{aligned} \quad (1.35)$$

Here \mathcal{A} is proportional to the Stokes parameter given by $\langle \mathcal{E}_l^2 \rangle - \langle \mathcal{E}_r^2 \rangle$, where \mathcal{E}_l and \mathcal{E}_r are the components of the electric field written the circular basis defined by $\hat{l} = (\hat{x} + i\hat{y})/\sqrt{2}$. The Stokes parameter \mathcal{A} is normalized so that $\mathcal{A} = +1$ for left-hand circularly polarized light. θ_k is the angle between the wave vector and the quantization axis (established by an external magnetic field \mathbf{B}). And ϕ is given by $\cos \phi = \frac{\langle (\mathcal{E} \cdot \mathbf{B})^2 \rangle}{\langle B^2 \rangle \langle \mathcal{E}^2 \rangle}$. The m_F and orientation independent parameters $\alpha^{(0)}(\omega)$, $\alpha^{(1)}(\omega)$, and $\alpha^{(2)}(\omega)$ are the scalar, vector, and tensor

polarizabilities, respectively, and are given by [23, 24, 25]

$$\alpha^{(0)} = \alpha_0 \frac{1}{\sqrt{3}} \quad (1.36)$$

$$\alpha^{(1)} = -\alpha_1 \sqrt{\frac{F}{2(F+1)}} \quad (1.37)$$

$$\alpha^{(2)} = -\alpha_2 \sqrt{\frac{2F(2F-1)}{3(F+1)(2F+3)}} \quad (1.38)$$

where α_p is given by

$$\alpha_p = \frac{1}{\hbar} \sqrt{\frac{2p+1}{2F+1}} \sum_{F'=F-1}^{F+1} (-1)^{F+F'} \left\{ \begin{matrix} 1 & 1 & p \\ F & F & F' \end{matrix} \right\} \times \sum_{n'} |\langle nF || \mathbf{d} || n'F' \rangle|^2 \left[\frac{1}{\omega_f - \omega_L} + \frac{(-1)^p}{\omega_f + \omega_L} \right] \quad (1.39)$$

The reduced electric dipole matrix elements $\langle nF || \mathbf{d} || n'F' \rangle$ are defined in Appendix B.

For atoms uniformly distributed among the m_F states, $\langle m_F \rangle = 0$ and $\langle m_F^2 \rangle = \frac{1}{3}F(F+1)$. Plugging these values into Eq. (1.35) gives $\langle \alpha(\omega) \rangle = \alpha^{(0)}(\omega)$. Thus, the vector and tensor terms only effect the polarizability when the atoms are in a specific m_F state.

1.2.3 Tune-Out Wavelength

Between any two resonances there exists a frequency such that $\alpha(\omega) = 0$. The cooresponding wavelength, $\lambda = 2\pi c/\omega$ is called a tune-out wavelength or magic-zero wavelength λ_0 . As discussed in Section 1.1, previous dynamic polarizability measurements have been limited by the ability to calibrate the intensity of the applied field. Measurements of the λ_0 are ideal due to their extremely weak intensity dependence.

The intensity dependence of the dynamic polarizability can be found by extending the Time-Independent Perturbation expansion in Section 1.2.1 to fourth order. The fourth

order correction to the quasienergy is given by [23]

$$\epsilon_n^{(4)} = -\frac{1}{4!}\gamma_n(\omega)\langle\mathcal{E}^4\rangle \quad (1.40)$$

where $\gamma_n(\omega)$, known as the hyperpolarizability, is given by [23]

$$\gamma_n(\omega) \approx \frac{1}{6\hbar^3} \sum_f \frac{|\langle\psi_0|\mathbf{d}|\psi_f\rangle|^4}{(\omega_f - \omega_L)^3} \quad (1.41)$$

The hyperpolarizability effectively shifts the polarizability by

$$\Delta\alpha(\omega) \approx -\frac{1}{8}\gamma_n(\omega)\frac{I}{c\epsilon_0} \quad (1.42)$$

where we used $\langle\mathcal{E}^4\rangle = 3/8|\mathcal{E}^4|$ to write the hyperpolarizability in terms of I . To calculate the measurement's dependence on intensity, we calculate $\Delta\alpha$ and compare this to the polarizability's sensitivity to wavelength, given by $\frac{d\alpha}{d\lambda}$. For the tune-out wavelength between the $5P_{1/2}$ and $5P_{3/2}$ manifolds, $\Delta\alpha \approx 1.0 (10^{-10}) \frac{\text{a.u.}}{\text{W/m}^2}$. At this same wavelength, $\frac{d\alpha}{d\lambda} \approx 2.5 \frac{\text{a.u.}}{\text{pm}}$. In our measurement of the tune-out wavelength, a 20 mW laser with a 30 μm beam waist was used to provide the Stark shift. At the peak intensity, the hyperpolarizability is $\Delta\alpha \approx 1.4 (10^{-3})$ a.u., resulting in a 0.5 fm shift to the tune-out wavelength. Since our tune-out wavelength measurement has an uncertainty of approximately 30 fm, the shift caused by the hyperpolarizability is negligible.

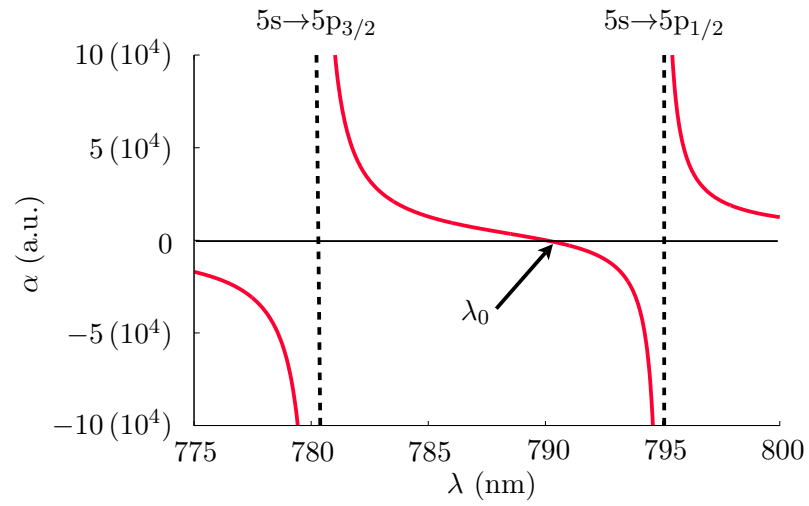


Figure 1.1: Tune-out wavelength between the D_1 and D_2 lines of ^{87}Rb .

Chapter 2

BEC Interferometer Apparatus

In this section, I will outline the procedure we use to make a BEC interferometer. A brief overview: we start by creating a Bose-Einstein condensate (BEC) which is then transferred to a magnetic trap, called a waveguide, in which our experiments are performed. A short off-resonant laser pulse is used to split the BEC into two packets. The energy of one of the packets is altered in a controlled way, inducing a phase shift in this packet. The packets are recombined, and the phase difference between the two packets of atoms is measured.

2.1 BEC Creation

In this section I will briefly outline how BEC is created in the lab. A detailed discussion of our BEC creation process can be found in the thesis of Jessica Reeves [26].

2.1.1 Laser Cooling & Magneto-Optical Trap

Our experiments are performed under vacuum. A thermal vapor of Rb atoms is maintained through the use of a dispenser, while an ion pump keeps the pressure at approximately 10^{-9} torr. Atoms from this background vapor are trapped and cooled inside a Magneto-Optical Trap (MOT). MOTs have been extensively studied and are widely used in cold

atom experiments. Therefore I will only briefly discuss the mechanisms responsible for the cooling and trapping of atoms inside a MOT, for additional details see Ref. [27]. In the reference frame of a moving atom, the wavelength of light is shifted due to the Doppler Effect. As a result, atoms moving towards light that is tuned red of an atomic resonance see the light shifted closer to resonance. In this scenario, the momentum transferred to the atom reduces the atom's kinetic energy. This phenomenon is known as Doppler laser cooling.

In a MOT, three pairs of red detuned counter propagating beams intersect over a region of space. Atoms in this region experience Doppler laser cooling regardless of the direction of the atom's motion. Confinement is achieved through magnetic field and polarization effects. A pair of coils in an anti-Helmholtz configuration create a magnetic field minimum at the center of the MOT. When an atom moves away from the MOT center, it experiences greater Zeeman splitting. For an appropriate choice of circularly polarized light, the atom is Zeeman shifted closer to resonance for light that tends to push it back towards the center of the trap.

In our experiment the cooling lasers are red detuned from the $5S_{1/2}, F = 2 \rightarrow 5P_{3/2}, F' = 3$ resonance for ^{87}Rb by about 20 MHz. An additional beam locked to the $5S_{1/2}, F = 1 \rightarrow 5P_{3/2}, F' = 2$ resonance "repumps" atoms that decay from the $5P_{3/2}, F' = 3$ state into the $5S_{1/2}, F = 1$ state.

2.1.2 Optical Pumping & Magnetic Trap

As atoms collect inside the MOT, the cloud of trapped atoms becomes optically thick, limiting the temperatures that we can achieve. To overcome this limit, we increase the detuning of our cooling laser by 24 MHz for 10 ms. Finally, the magnetic field is turned off for 15 ms, allowing the atoms cool further through optical molasses. Through these combined laser cooling techniques we cool billions of atoms to a temperature of around $250 \mu\text{K}$.

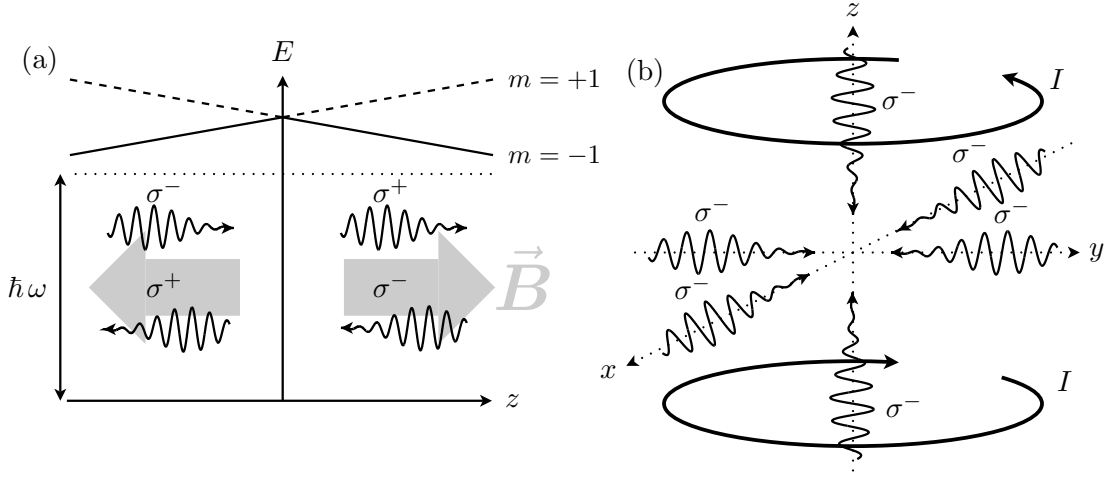


Figure 2.1: The spatially dependent Zeeman effect brings light that pushes the atoms towards the center of the trap closer to resonance. For consistency, m_F describes the projection of the angular momentum onto the quantization axis defined by \mathbf{B} . Another convention commonly used defines m_F as the projection onto the positive z-axis. For the convention used here, the spin of the photon with respect to the quantization axis of the atom reverses when crossing through the center of the trap, because the direction of the magnetic field reverses at this point. Because magnetic moment of the atom $\boldsymbol{\mu}$ follows \mathbf{B} , the Zeeman shift depends only on the magnitude of the magnetic field, resulting in the symmetric energy level diagram shown above. When using the other convention, the spin of the photon is unchanged when passing through the MOT, as the quantization axis always points in the same direction. However, because magnetic moment of the atom $\boldsymbol{\mu}$ follows \mathbf{B} , the m_F state of an atom changes sign when passing through the center of the MOT. This results in an antisymmetric energy level diagram.

To cool the atoms further another cooling technique is required: evaporative cooling. In our experiment the atoms are evaporated in a magnetic trap. A magnetic trap uses the force associated with the Zeeman shift of the ground state valence electron to trap atoms in a local magnetic field minimum. Inside a magnetic field, atoms experience a force of

$$\mathbf{F} = g_F m_F \mu_B \nabla |B| \quad (2.1)$$

For atoms in $5S_{1/2}$, $F = 2$ state, the Landé g_F -factor is approximately $1/2$.

To maximize the strength of the magnetic force, our atoms are optically pumped into the $|F = 2, m = 2\rangle$ state. To accomplish this, we first turn off the cooling light and

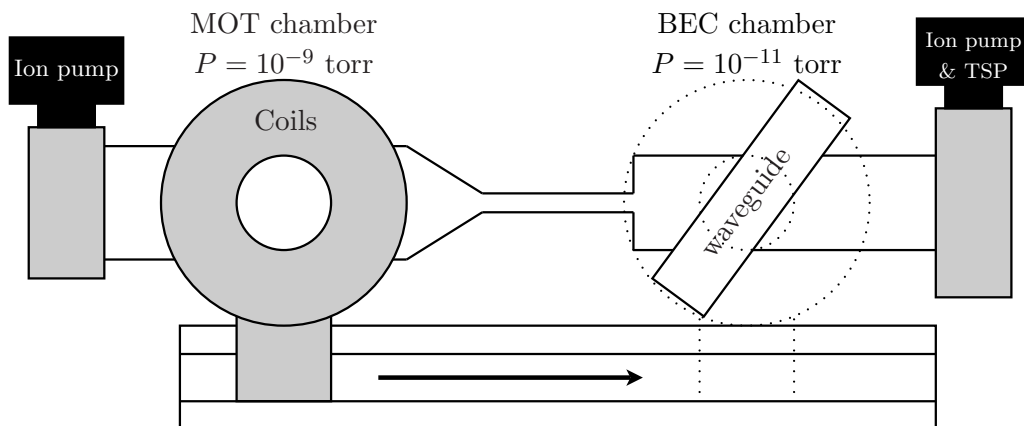


Figure 2.2: Two vacuum chambers are connected by a thin tube. Rb atoms from a thermal vapor in the MOT chamber are trapped and cooled in a MOT. These atoms are transferred to a magnetic trap. The coils generating the trapping field physically move along a track, carrying the atoms to the BEC chamber which has a pressure of around 10^{-11} torr.

magnetic field from the MOT. We then apply a bias magnetic field along with σ^+ light that is tuned to the $5S_{1/2}, F = 2 \rightarrow 5P_{3/2}, F' = 2$ transition. As the atoms cycle between $F = 2$ and $F' = 2$, the m level of the atom gradually increases. Because the light is tuned to the $F' = 2$ excited state, there is no $m' = 3$ excited state. As a consequence, atoms in the desired $|F = 2, m = 2\rangle$ state no longer interact with the σ^+ light.

After optically pumping the atoms, we use the magnetic field generated by the same coils used in the MOT to trap the atoms in a spherical quadrupole

$$\mathbf{B}_{sq} = B'_x(-x \hat{x} - y \hat{y} + 2z \hat{z}) \quad (2.2)$$

A magnetic field gradient of $B'_x \approx 190$ G/cm is achieved by increasing the current to 700 A. Once the atoms are trapped, the coils generating the trapping field physically move along the length of our apparatus carrying the atoms to a second vacuum chamber which has a pressure of around 10^{-11} torr.

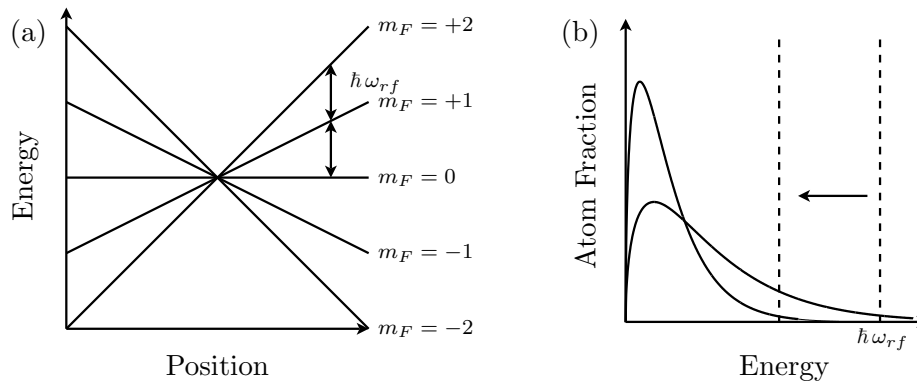


Figure 2.3: (a) An rf field resonant with the $m_F = 2 \rightarrow m_F = 1$ transition for atoms experiencing a large Zeeman shift, selectively removes high-energy atoms from the magnetic trap. (b) As the atoms rethermalize to lower temperatures, the rf frequency is reduced.

2.1.3 Forced RF Evaporation

After the atoms are transferred to the BEC chamber, we use forced rf evaporation to cool the atoms further. This method takes advantage of the fact that high-energy atoms may travel further from the magnetic trap center where they experience larger Zeeman shifts. An rf field resonant to the $m_F = 2 \rightarrow m_F = 1$ transition for atoms experiencing a large Zeeman shift is applied. High energy atoms absorb multiple photons from the rf field, transferring the atoms from $m_F = 2$ to the $m_F = 1, 0, -1, -2$ states. As a result, high energy atoms are selectively removed from the trap. As the atomic cloud rethermalizes to lower temperatures, the rf frequency is reduced. The process continues until a BEC is formed.

2.1.4 Time-Orbiting Potential Trap

During the evaporation process, the atoms spend more time near the magnetic field zero. Since the magnetic field defines the quantization axis of the atoms, atoms near the magnetic field zero lose their spin orientation, allowing an atom to transition from $m_F = 2$ to a non-trapping or anti-trapping state. This phenomenon, known as a Majorana flip, leads

to atom lose in the magnetic trap. To avoid this lose, we use a time-orbiting potential (TOP) trap. A TOP trap uses a time-dependent magnetic field such that the atoms experience a force that is related to the time-average of the magnetic field. This allows the atoms to be trapped in the minimum of the time-averaged magnetic field, while moving the instantaneous magnetic field zero along a path which avoids the trapped atoms.

The TOP trap is created by adding a spatially uniform rotating bias field to the static quadrupole field of the magnetic trap.

$$\mathbf{B}_0 = B_0 (\hat{x} \cos(\Omega t) + \hat{z} \sin(\Omega t)) \quad (2.3)$$

where $B_0 = 20$ Gauss and $\Omega = 2\pi \cdot 12.82$ kHz. The bias field frequency Ω is chosen to be smaller than the Larmor frequency (≈ 10 MHz) so the atoms spins adiabatically follow the field, while being larger than the frequency of the atomic motion (≈ 10 Hz) so the atoms feel a time-averaged potential. The magnitude of the TOP trap field is given by

$$|\mathbf{B}| = [B_0^2 + B_x' (x^2 + y^2 + 4z^2) - 2B_0 B_x' x \cos(\Omega t) + 4B_0 B_x' z \sin(\Omega t)]^{1/2} \quad (2.4)$$

Expanding to second-order and taking the time-average gives

$$\langle |\mathbf{B}| \rangle = B_0 + \frac{B_x'}{B_0} \left(\frac{1}{4} x^2 + \frac{1}{2} y^2 + z^2 \right) \quad (2.5)$$

resulting in trap frequencies

$$\omega_x^2 = \frac{1}{2} \frac{\mu B_x'^2}{m B_0}, \quad \omega_y^2 = \frac{\mu B_x'^2}{m B_0}, \quad \omega_z^2 = 2 \frac{\mu B_x'^2}{m B_0} \quad (2.6)$$

The last stages of evaporation are performed in the TOP trap.

2.2 BEC Wave Guide

While the TOP trap holds the BEC against gravity and provides spatial confinement, it has several limitations which make it unsuitable for our interferometry experiments. Firstly, the static spherical quadrupole field of the TOP trap is susceptible to static environmental fields, whereas potentials created by alternating fields are only susceptible to components of the environmental field which are harmonics of the field frequency. Secondly, the tight confinement of the TOP trap results in large atomic interactions which limit the coherence time of our condensate.

With these limitations in mind, we load the BEC into a weakly confining time-averaged potential created using ac magnetic fields. To support the BEC against gravity while creating a weakly confining trap, we engineered a field which exerts an upward force on the BEC. Since the atoms are in a low-field-seeking state, this force may be realized by creating a field in which the magnetic field zero remains in a plane above the atoms. This is accomplished by adding an oscillating linear quadrupole field to a rotating bias field.

The spatially uniform rotation bias field used in the TOP trap and given by Eq. (2.3) is added to an oscillating linear quadrupole field given by

$$\mathbf{B}_{lq} = B'_{lq} (x \hat{x} - z \hat{z}) \sin(\Omega t) \quad (2.7)$$

The linear quadrupole is phase-locked to, and oscillates at the same frequency as, the Bias. A pair of coils oriented along the weakly confining y-axis of the guide were added to provide additional confinement. These coils were driven at the incommensurate frequency $\varpi = 2\pi \cdot 1.0$ kHz. The field from these coils is written as

$$\mathbf{B}_y = B'_x (-x \hat{x} + 2y \hat{y} - z \hat{z}) \sin(\varpi t) \quad (2.8)$$

where $B'_x \approx 2.5\text{G/cm}$. Expanding the time-average of the magnitude of the field to second

order gives

$$|\mathbf{B}| \approx B_0 - \frac{B'_{lq}}{2} z + \frac{1}{16 B_0} (2 B_x'^2 + 3 B_{lq}'^2) x^2 + \frac{B_x'^2}{B_0} y^2 + \frac{1}{16 B_0} (2 B_x'^2 + B_{lq}'^2) z^2 \quad (2.9)$$

The linear quadrupole gradient is chosen to perfectly cancel the gravitational force. Therefore we can show that

$$\begin{aligned} \frac{\mu B'_{lq}}{2} &= m g \\ B'_{lq} &= \frac{2 m g}{\mu} \end{aligned} \quad (2.10)$$

which gives $B'_{lq} \approx 30$ G/cm. Solving for the resulting trap frequencies gives

$$\omega_x^2 = \frac{\mu}{8 m B_0} (2 B_x'^2 + 3 B_{lq}'^2), \quad \omega_y^2 = \frac{2 \mu B_x'^2}{m B_0}, \quad \omega_z^2 = \frac{\mu}{8 m B_0} (2 B_x'^2 + B_{lq}'^2) \quad (2.11)$$

which gives $\omega_x \approx 2\pi \cdot 4$ Hz, $\omega_y \approx 2\pi \cdot 1$ Hz, $\omega_z \approx 2\pi \cdot 3$ Hz.

2.3 Bragg Splitting & Reflecting

In the sections above, I describe the procedure used to create and hold a BEC. Because the vast majority of atoms in a BEC occupy the ground state of the confining potential, the BEC provides a coherent source of atom waves. To implement an interferometer, we must split this wave into two independent waves which transverse different paths. Once the waves are split, we must coherently recombine the waves so that they overlap and interfere. In an optical interferometer, splitting and recombining can be accomplished via a beam-splitter and mirrors. In our experiment, momentum transfer from an off-resonant standing wave is used to split and recombine the atom waves. The timing and intensity of a standing wave was chosen to optimize the fidelity of the splitting and reflecting operations. Details of the optimization, which was calculated by Jeremy Hughes and John Burke, were

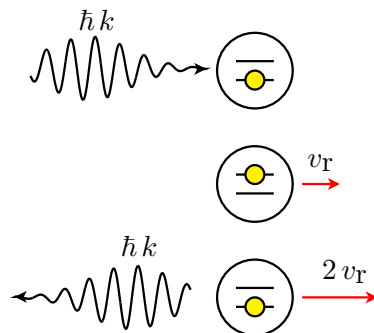


Figure 2.4: The atom-field interaction responsible for the Bragg Splitting can be understood as an absorption followed by stimulated emission.

published here [28]. As the theory and details of Bragg diffraction are discussed elsewhere [13, 29, 30, 28], I will provide only a brief description of the process.

The interaction between the atoms and the laser field during the splitting pulse can be understood as absorption from one beam followed by stimulated emission into the opposing beam. Since each photon carries momentum $\hbar k$, the atom receives a total momentum transfer of $2\hbar k$, corresponding to a velocity of 11.7 mm/s. A result of symmetry: the atoms split into two packets of equal size traveling in opposite directions. Bragg reflection occurs through two absorption-emission cycles, transferring a total momentum of $4\hbar k$ and changing the momentum of the atoms from $\pm 2\hbar k$ to $\mp 2\hbar k$.

The idealized split operation perfectly couples the state describing a packet of atoms at rest $|0\rangle$ to a superposition of states describing atoms moving in opposite directions with momentum $\pm 2\hbar k$. As a result, the split operation can be represented mathematically of as a unitary operator with the following properties

$$\begin{aligned}
 U_{\text{Split}} |0\rangle &= |\text{Split}\rangle \stackrel{\text{def}}{=} \frac{1}{\sqrt{2}} (|2\hbar k\rangle + |-2\hbar k\rangle) \\
 U_{\text{Split}} |\text{Split}\rangle &= |0\rangle
 \end{aligned} \tag{2.12}$$

Similarly the reflect operation can be represented mathematically as

$$U_{\text{Reflect}}|\pm 2\hbar k\rangle = |\mp 2\hbar k\rangle \quad (2.13)$$

Over the course of an interferometer measurement, a phase difference $\Delta\phi$ develops between the two packets of atoms. The resulting state may be written as $|\phi\rangle = 1/\sqrt{2}(|2\hbar k\rangle + e^{i\Delta\phi}|-2\hbar k\rangle)$. The phase difference between the two packets is measured by applying a split pulse when two packets are overlapping. Since $U_{\text{Split}}|\text{Split}\rangle = |0\rangle$, the fraction of atoms that come to rest after the recombination pulse is applied is given by

$$\begin{aligned} \frac{N_0}{N} &= |\langle \text{Split} | \phi \rangle|^2 \\ &= \frac{1}{4} |1 + e^{i\Delta\phi}|^2 \\ &= \cos^2\left(\frac{\Delta\phi}{2}\right) \end{aligned} \quad (2.14)$$

Notice that the equation for N_0/N is even. As a result, a measurement of N_0/N is unable to determine the sign of phase shift. We resolve this issue by introducing a $\pi/2$ phase shift in the final recombination pulse. This phase shift is achieved by slightly shifting the frequency of the recombination pulse.

2.4 Confinement Effects & Interferometer Symmetry

After we split the atoms, atoms in one of the packets are manipulated in a controlled fashion while the atoms in the other packet are left undisturbed. Any shift in the energy of the manipulated atoms will alter the phase development of this atom wave packet. When the two packets are recombined, the phase difference between the two packets is measured, revealing information about this energy shift.

Manipulating the phase of the atoms in one packet in a controlled way requires that the atoms repeatably travel along the same trajectory following the split pulse. The

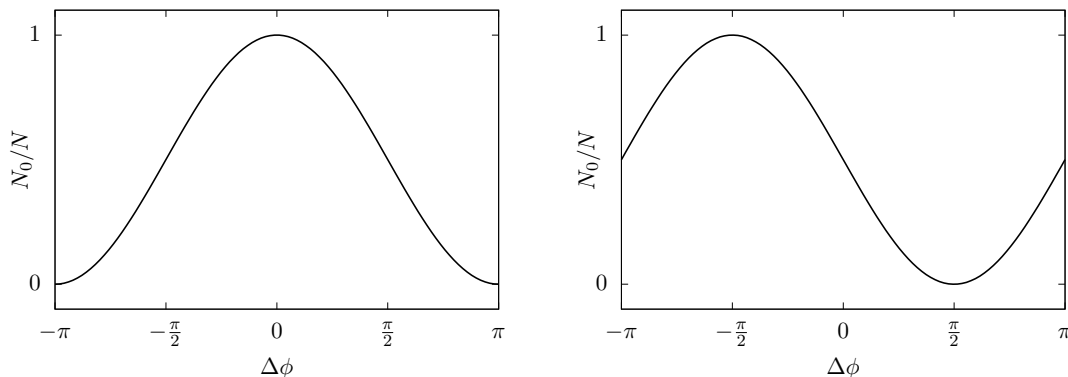


Figure 2.5: The graph on the left shows how N_0/N changes when atoms in one packet experience a phase shift $\Delta\phi$ and no additional phase shift is applied during the recombination pulse. Notice that N_0/N decreases from a maximum value of 1.0 for both positive and negative phase shifts, making it impossible to determine the sign of $\Delta\phi$. The graph on the right shows the N_0/N dependence on $\Delta\phi$ when an additional phase shift of $\pi/2$ is applied during the recombination pulse. Note that, for the graph on the right, the sign of $\Delta\phi$ is easily determined through the measurement of N_0/N .

repeatability of the trajectory can be improved by increasing the waveguide confinement along the two directions perpendicular to the motion given to the atoms by the split pulse. Moreover, to manipulate the phase of only one of the atom wave packets, the packets must completely spatially separate before the reflect pulse is applied. To ensure that the momentum provided by the split pulse is sufficient to spatially separate the two packets, a weaker confinement is used along the direction that the atoms move. In an ideal waveguide, there would be no confinement along the direction in which the atom waves are being guided. However, three practical concerns prevent free motion along the waveguide axis: Firstly, edge effects caused by the finite length of the waveguide generate some confinement along the axis of the guide. Second and thirdly, increasing the confinement along the axis of the waveguide spatially confines atoms to a manageable packet size, while also improving the repeatability of the atoms' initial position.

In an ideal atom wave interferometer, a uniform phase builds up across the length of an individual atom wave packet so that, when the two packets overlap, the phase difference between overlapping portions is the same throughout entire packet. However,

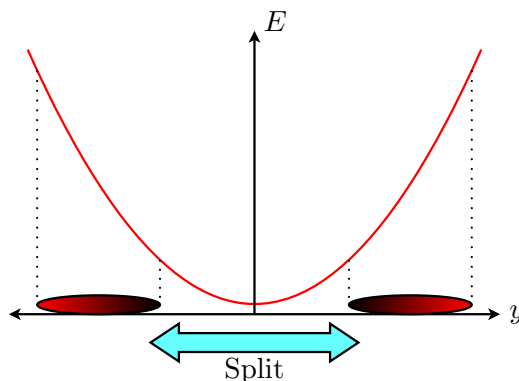


Figure 2.6: Confinement along the axis of the waveguide causes the opposite ends of the atom wave packet to experience different potential energies, thereby inducing a phase gradient across the length of the atom wave packet.

confinement along the axis of the waveguide results in a phase gradient across the length of the atom wave packet. As a result, different parts of the two atom wave packets interfere differently. Because the phase difference is found by measuring the fraction of the atoms that return to rest after the recombination split pulse, large phase gradients eventually cause the interference pattern to “wash-out”, resulting in a N_0/N fraction of 0.5 in every interferometry measurement.

To minimize the effect of this phase gradient, a symmetric trajectory is employed so that each individual atom wave packet experiences canceling positive and negative gradients. The symmetric trajectory used in this experiment is achieved by performing the split-reflect interferometer described in Section 2.3, however, after the reflect pulse, the the atom wave packets are allowed to pass through each other (rather than being recombined). As the atom wave packets pass through each other and move into the other side of the waveguide, they experience a phase gradient which has the opposite sign as the phase gradient felt by the atom wave packet immediately after the split pulse. A second reflect pulse brings the two atom wave packets back together and ensures a symmetric trajectory.

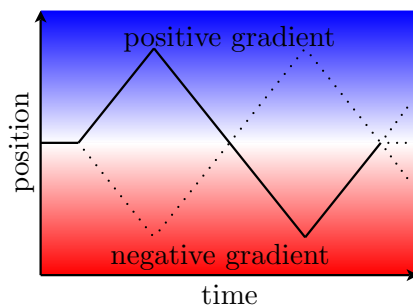


Figure 2.7: Symmetric trajectories cause each atom wave packet to experience canceling positive and negative phase gradients. Blue and red in the figure above indicate positive and negative phase gradients respectively.

2.5 Absorption Imaging

The fraction of atoms that come to rest is determined through absorption imaging. In absorption imaging, atoms absorb light from a short pulse of resonant light, thereby casting a shadow in the imaging beam. The plane that the atoms are in is imaged onto a CCD. Thus, the CCD captures an image of the spatial intensity profile of the beam in the plane of the atoms. Absorption from the atoms is identified by comparing images of beam’s intensity profile with and without the atoms in the waveguide. In our experiment, absorption imaging was setup along both the x and z axes of the waveguide.

Three raw images are used to create a composite image which shows the fraction of the imaging light absorbed by the atoms. A “Background” image, taken in the absence of the imaging light pulse, is used to compensate for leakage light and CCD offset. An “Atoms” image is created by imaging the intensity profile of the resonant imaging light when atoms are present in the imaging beam’s path. And a “No atoms” image shows the spatial intensity profile of probe light in the absence of atoms. The final composite image is created according to the following formula

$$\text{final image} = \frac{\text{Atoms} - \text{Background}}{\text{No Atoms} - \text{Background}} \quad (2.15)$$

A fitting routine uses this composite image to determine fraction of the atoms that return to rest.

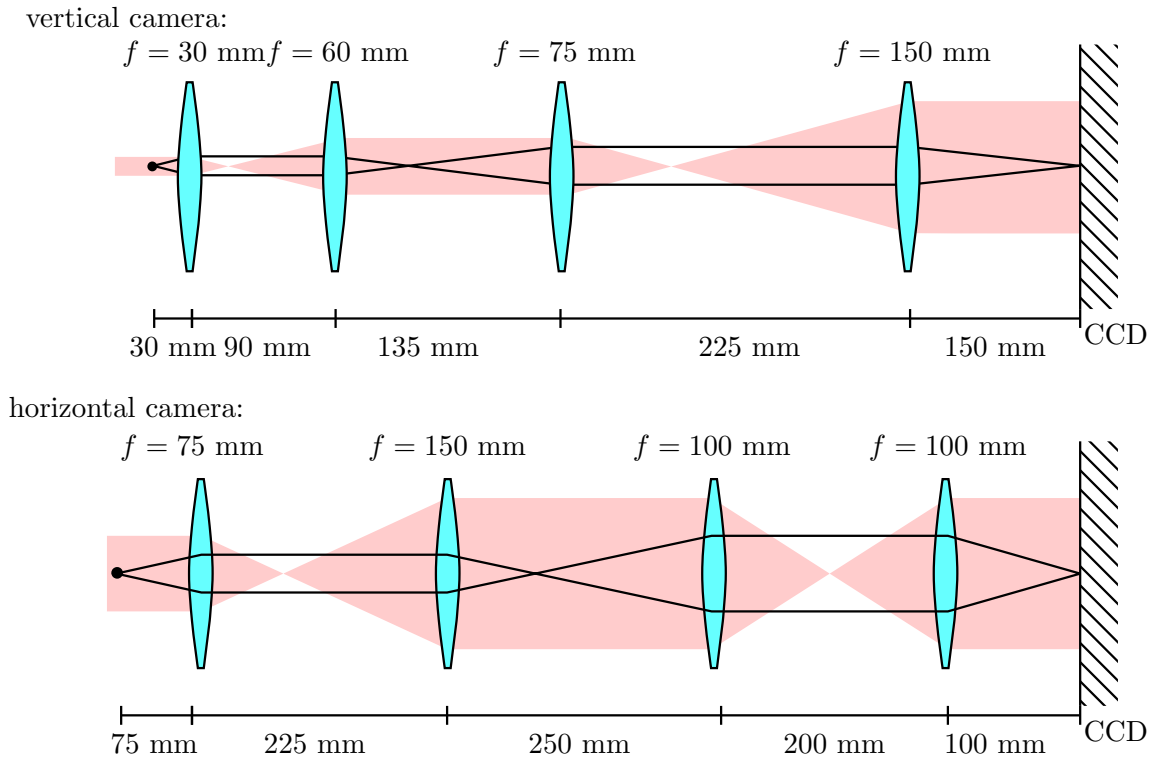


Figure 2.8: Schematic showing the lens configuration used in the vertical and side absorption imaging. Infinity-corrected achromatic lenses are used throughout both imaging setups. In the vertical setup the atoms are imaged onto an Apogee AP47P camera, which has a resolution of 1024×1024 and a pixel size of $13 \mu\text{m}$. The optics provide a 4x magnification resulting in imaging resolution of approximately 307 px/mm . In the horizontal setup the atoms are imaged onto a Pixis 1024 camera, which also has a resolution of 1024×1024 and a pixel size of $13 \mu\text{m}$. The optics provide a 2x magnification resulting in imaging resolution of approximately 154 px/mm . The red shaded region shows the ray diagram of the absorption laser, while the solid black lines show the ray diagrams of the absorption image of the atoms.

Chapter 3

Tune-Out Wavelength Experiment

In this chapter, I will outline the procedure we used to measure the tune-out wavelength.

3.1 Overview

Our tune-out wavelength measurements essentially consist of a series dynamic polarizability measurements made over a range of wavelengths close to, and on both sides of, the tune-out wavelength. The tune-out wavelength is determined by interpolating this data to find the wavelength at which the dynamic polarizability is zero. Each dynamic polarizability measurement was made by measuring the phase difference that developed between two atom packets when one of the atom packets passes through an applied laser field. The phase difference that develops between the two atom packets is related to the applied field intensity by

$$\Delta\phi = \int -\frac{\hbar}{2c\epsilon} \alpha(\omega) I dt \quad (3.1)$$

To avoid errors which arise from the uncertainty in the intensity of the applied field, the measurement was repeated for a range of field intensities while keeping the wavelength fixed. Because the applied field intensity is difficult to measure, we measured the total power of the applied field for each phase measurement. The total power of the applied

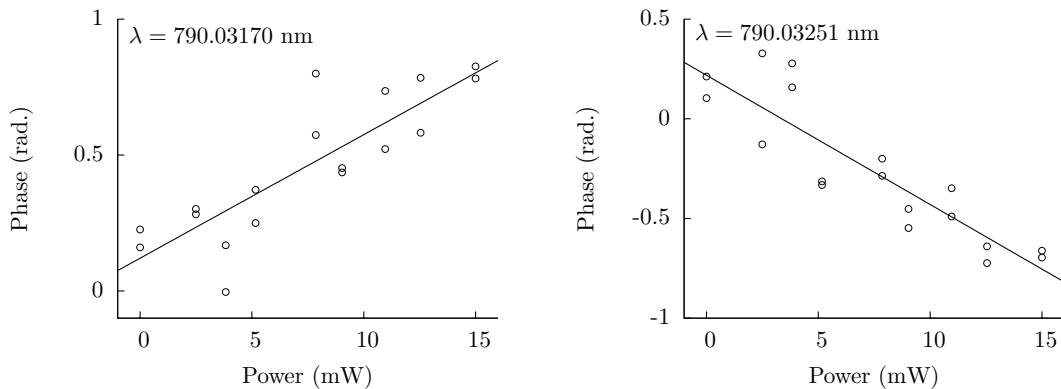


Figure 3.1: Phase shift at $\lambda = 790.03170$ nm and 790.03251 nm. The intercept $Phase = 0$ rad. represents the phase shift at which $N_0/N = 0.5$. Due to the phase encoded onto the atoms by the recombination Bragg pulse (see Sec. 2.3), the point at which $Phase = 0$ rad. is somewhat arbitrary.

field was varied from zero to 18 mW using an AOM. Since the intensity of the applied field is proportional to its total power, the phase difference given by Eq. (3.1) may be rewritten in terms of our measured quantities as a simple proportionality relation

$$\Delta\phi = \kappa P \quad (3.2)$$

where κ is proportional to the dynamic polarizability. The measured phase differences and laser powers were fit to a straight line using the least squares method. The one sigma uncertainty in the fit parameter is treated as our uncertainty in κ . The wavelength of the applied field was measured periodically during the data collection; the standard deviation of the measured wavelengths is treated as the random uncertainty in the wavelength for the κ measurement. The entire process of measuring κ was repeated for a range of wavelengths close to, and on both sides of, the tune-out wavelength. From this data we plot κ versus λ . Using a linear fit, we determine the wavelength λ_0 where κ , and thus α , equals zero. We use the fit uncertainty in λ_0 as the random uncertainty in the measured value of the tune-out wavelength.

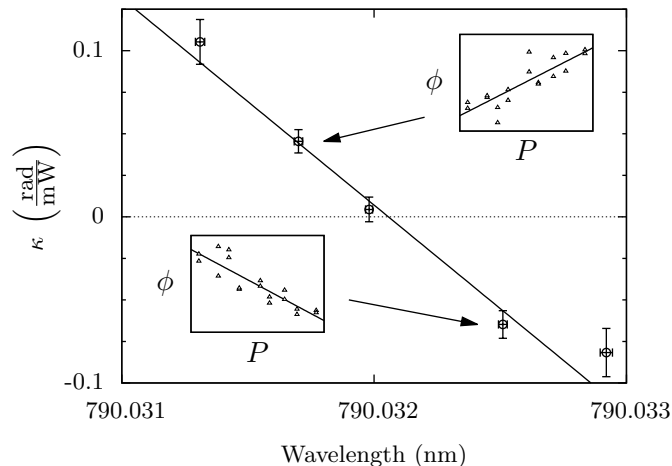


Figure 3.2: Tune-out wavelength data for light linearly polarized along the x-axis.

3.2 Detailed Experimental Procedure

The atoms are loaded into a waveguide with a harmonic trapping potential with frequencies $\omega_x \approx 2\pi \cdot 5.1$ Hz, $\omega_y \approx 2\pi \cdot 1.1$ Hz, and $\omega_z \approx 2\pi \cdot 3.2$ Hz. The atoms are split, via Bragg scattering, into two equal packets which travel in opposite directions along the weakly confining y-axis of the waveguide. After the split pulse, the atoms are moving at a speed of 11.7 mm/s. Immediately following the split pulse, a laser field is applied along the trajectory of one of the two atom packets. One of the atom packets passes through the applied laser field, accumulating a phase shift as a result of the ac Stark shift. Ten milliseconds after the split pulse, the motion of both atom packets is reversed via a reflection pulse. When the atom packets return to their initial position, 20 ms after the initial split pulse, the applied laser field is removed. As described in Section 2.4, we minimize spatial phase gradients, which form across the length of the atom packets, by allowing the atoms to pass through each other and trace out symmetric trajectories. When the atom packets return to their initial position, a second split pulse is applied. A fraction of the atoms return to rest, while the remaining atoms continue their trajectories. The atom packets which remain in motion continue to separate until they become spatially

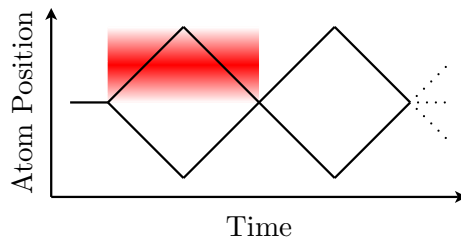


Figure 3.3: Atom-wave packet trajectories during a typical polarizability measurements. The timing and position of the applied field is denoted by the shaded region within the graph.

distinct from the atoms at rest. The three distinct atoms packets are then imaged via absorption imaging. The fraction of the atoms which return to rest is then determined by a program which analyzes the absorption image. As described in Section 2.3, the fraction of atoms which return to rest is related to the phase difference between the two packets according to Eq. (2.14).

3.2.1 Stark Beam Alignment

Recall that the atom-light interaction energy is proportional to the intensity of the applied light

$$\Delta E = -\frac{1}{2c\epsilon}\alpha(\omega)I \quad (1.3)$$

To increase the sensitivity of our interferometer, we focused the applied beam onto the plane of the atom's motion, thereby maximizing its intensity for a given power. In our experiment we engineered the beam to have a waist of approximately $30\ \mu\text{m}$. This was chosen as the smallest feasible waist size, as the atom packets have a width of $13\ \mu\text{m}$ in the direction perpendicular to their motion. The small beam waist presented two challenges for our experimental design: Firstly, the small beam size requires a method for precisely aligning the applied beam onto the trajectory of the atom packet. Secondly, the atom trajectory must be repeatable to better than $30\ \mu\text{m}$.

To align the Stark beam along the trajectory of the atom packet, the vertical imaging

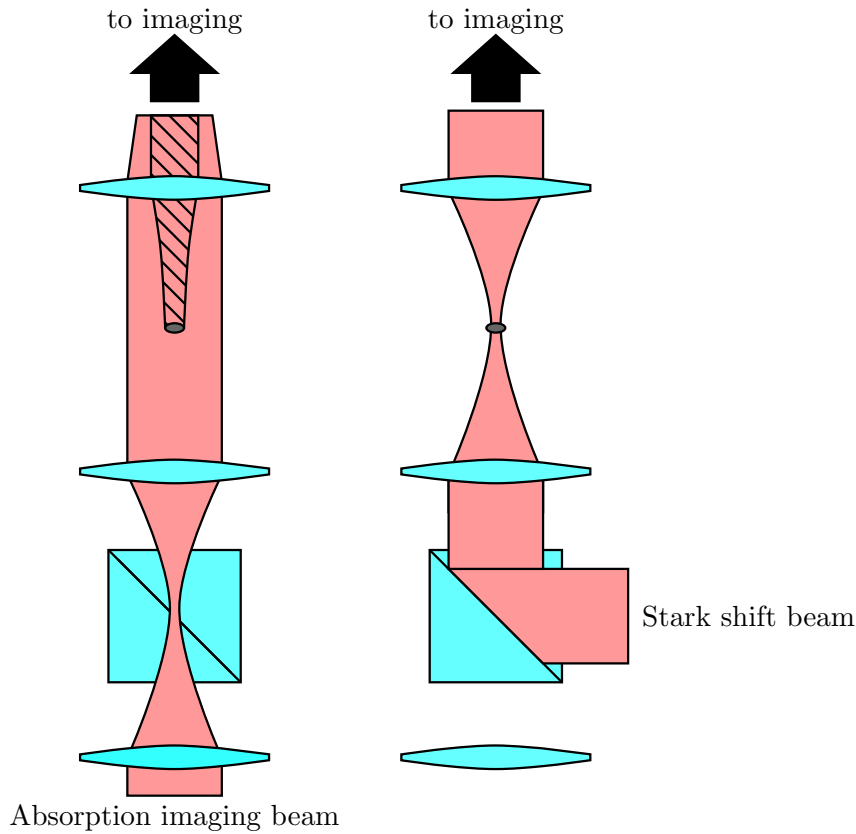


Figure 3.4: Schematic of Atom & Stark Beam Imaging.

system was used to image both the atoms as well as the Stark beam. Using the imaging scheme illustrated in Figure 3.2.1, we imaged the position of the atoms as well as the position of the Stark beam using the same camera and imaging optics. Because absorption imaging requires a collimated resonant beam, while the tune-out wavelength measurement requires a focused off-resonant beam, the two beams follow separate paths before being combined via a polarizing beam splitting cube and directed into the imaging optics. Due to thermal drift, the Stark beam was realigned at the start of each day, before the tune-out wavelength measurements.

In section 3.1, I explain that the tune-out wavelength is found by measuring an atom-wave packet's phase sensitivity to the intensity of an applied Stark beam. This phase sensitivity is found by measuring the slope of the accumulated phase versus the total

power of the applied Stark beam, which is controlled via an AOM. Because we are unable to image the Stark beam and atoms simultaneously during the experiment, we are unable to correct for variations in the applied intensity due to shifts in the relative positions of the Stark beam and the atom-wave packet. As a result, these variations constitute an uncontrolled source of uncertainty in the intensity of the Stark beam. These intensity variations result in noise in the phase versus power data, and result in larger uncertainties in the measured values of κ .

One major source of fluctuations in the trajectories experienced by the atom-wave packets arise from the motion given to the atoms when being transferred into the waveguide. To minimize this motion, the position and tilt of the waveguide, as well as the rate at which the various fields ramp on and off, were carefully adjusted so that the time-averaged magnetic field minimum did not move during the transfer from the TOP trap into the waveguide. To further improve the repeatability of the atom-wave trajectories, additional confinement was provided along the weakly confining y axis of the waveguide using a pair of coils. These coils provided an AC magnetic field to minimize the effect of environmental fields. After optimization, the position of the split atom-wave packets were found to be repeatable to within $6\ \mu\text{m}$ in the direction perpendicular to the axis of the waveguide and $20\ \mu\text{m}$ in the along the weakly confining direction of the waveguide. Fluctuations in the position of the Stark beam were also measured, however these were found to be negligible.

3.2.2 Broadband Light

Another major concern is broadband light in the Stark beam. The Stark beam was produced by a home-built grating stabilized external-cavity diode laser. The diode, Thorlabs L785P090, was free-running near 783 nm. An external cavity pulled the laser to 790 nm. The scattering rate of the Stark beam near 790 nm was observed to be much higher than expected. The observation was consistent with the presence of broadband light over the

atomic resonances near 780 nm.

For light composed of a single wavelength, the scattering rate may be calculated as

$$R_s = \frac{\Gamma}{2} \left(\frac{\frac{I}{I_{\text{sat}}}}{1 + \frac{I}{I_{\text{sat}}} + 4 \left(\frac{2\pi\Delta}{\Gamma} \right)^2} \right) \quad (3.3)$$

where $\Delta = f - f_0$ is the detuning from resonance, Γ the natural linewidth of the transition, and I_{sat} is the saturation intensity. For the $5P_{3/2}$ transition, the linewidth is $2\pi \cdot 5.75$ MHz, the saturation intensity is approximately 36 W/m^2 , and the resonance is at 780.241 nm.

Observations of the Stark beam scattering rate were achieved by splitting atoms via Bragg scattering into two moving packets, such that one of the atom packets traveled through the Stark beam, while the other packet traveled away. The fraction of the atoms scattered by the Stark beam was determined by comparing the number of atoms in the two packets after one packet traveled completely through the Stark beam. This measurement was repeated for different Stark beam intensities. We expect 0.3% of the atoms to be scattered by a 7.6 mW Stark beam at 790 nm with a waist of $30 \mu\text{m}$; the measured fraction of the atoms scattered was 80%.

The increased scattering rate was found to be the result of broadband light near the $5P_{3/2}$ resonance. We came to this conclusion by comparing the scattering rates of the Stark beam with and without a band-pass filter, which transmitted light near the $5P_{3/2}$ resonance, while filtering light at 790 nm. While the band-pass filter transmitted approximately 3% of the overall Stark beam power, the scattering rate with the filter was approximately one-third of the unfiltered Stark beam scattering rate. The spectral transmission of the band-pass filter, along with the results of our scattering rate measurements are shown in Figure 3.5.

The scattering rate of a spectrum may be calculated by integrating over Eq. (5.1).

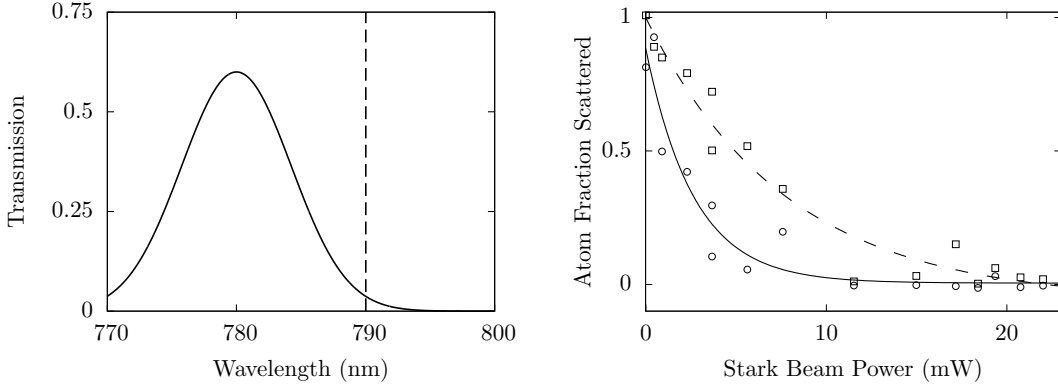


Figure 3.5: The graph on the left shows the spectral transmission of the band-pass filter used to investigate the unexpectedly high Stark beam scattering rate. The plots on the right show the fraction of atoms that remain after traveling through the Stark beam with (square) and without (circle) the band-pass filter.

For a low-intensity spectrum, we may ignore the I/I_{Sat} in the denominator.

$$R_s = \int \frac{\Gamma}{2} \left(\frac{\frac{S(\nu)}{I_{\text{Sat}}}}{1 + 4 \left(\frac{2\pi\Delta}{\Gamma} \right)^2} \right) d\nu \quad (3.4)$$

where S is the spectral intensity. If we model the broadband portion of the Stark beam as a uniform spectral intensity extending over the $5P_{3/2}$ resonance, we may approximate Eq. (3.4) by treating S as a constant and taking the integral from $-\infty$ to $+\infty$. In this case, Eq. (3.4) reduces to

$$R_s \approx \frac{1}{2} \left(\frac{\Gamma}{2} \right)^2 \left(\frac{S}{I_{\text{Sat}}} \right) \quad (3.5)$$

Using Eq. (3.5), we find that the power spectral density of the Stark beam near the $5P_{3/2}$ resonance is approximately $PSD \approx 4 \cdot 10^{-17} \text{ Hz}^{-1} \times P$, where P is the total power of the Stark beam.

Broadband light from the Stark beam is a major concern for two reasons: As described above, broadband light near the $5P_{3/2}$ resonance removes atoms from one arm of the interferometer, limiting our ability to perform interferometry measurements. Far more

serious, however, is the effect that broadband light has on our measured value of the tune-out wavelength. Recall that the interferometer measures a phase difference which is proportional to the time-averaged Stark shift given by Eq. (1.3). For broadband light with spectral intensity $S(\nu)$, the Stark shift may be calculated by integrating Eq. (1.3)

$$\langle \Delta E \rangle = \int -\frac{1}{2c\epsilon} \alpha(\nu) \langle S(\nu) \rangle d\nu \quad (3.6)$$

where the brackets indicate time-averaging over the atomic trajectory. To determine the effect that broadband light has on our measurement of the tune-out wavelength, we compare the Stark shift caused by the broadband light ΔE_{bb} to the derivative of the Stark shift caused by the main Stark beam light with respect to the frequency of the light $d(\Delta E)/d\nu$.

$$\Delta\nu = \frac{\Delta E_{\text{bb}}}{d(\Delta E)/d\nu} \quad (3.7)$$

For a non-uniform spectral intensity distribution near the $5P_{3/2}$ resonance, this shift is on the picometer scale.

To address this issue, the Stark beam was spectrally filtered by reflecting the light off a blazed grating with 1200 lines/mm, then focusing it through a lens with a 75 mm focal length, and finally directing this light through a $50\ \mu\text{m}$ diameter pinhole placed at the focus of the lens. Because the angle of the reflection off of the grating reflects depends on the wavelength of the light, only light with the desired wavelength will pass through the pinhole. To find the range of wavelengths accepted by the pinhole we relate the $d\theta$ caused by the grating to the displacement dy at the pinhole. This may be calculated via ray transform matrix analysis starting from the grating. The ray transform matrix for the

light at the pinhole is given by

$$\begin{aligned}
 \begin{pmatrix} y' \\ \theta' \end{pmatrix} &= \begin{pmatrix} 1 & f \\ 0 & 1 \end{pmatrix} \begin{pmatrix} 1 & 0 \\ -\frac{1}{f} & 1 \end{pmatrix} \begin{pmatrix} 1 & d \\ 0 & 1 \end{pmatrix} \begin{pmatrix} y \\ \theta \end{pmatrix} \\
 &= \begin{pmatrix} 0 & f \\ -\frac{1}{f} & 1 - \frac{d}{f} \end{pmatrix} \begin{pmatrix} y \\ \theta \end{pmatrix} \\
 &= \begin{pmatrix} f\theta \\ -\frac{y}{f} + \left(1 - \frac{d}{f}\right)\theta \end{pmatrix} \tag{3.8}
 \end{aligned}$$

Thus the beam displacement at the pinhole is given by $dy = f d\theta$. For light reflected from a grating, $d\theta$ can be related to $d\lambda$ by

$$d\theta = \frac{d\lambda}{d \cos \theta} \tag{3.9}$$

where θ is given by $\sin \theta = \frac{\lambda}{d}$.

For a 50 mm pinhole, $d\lambda = 176$ pm. In the worst-case scenario, the pinhole transmits light starting -176 pm from the tune-out wavelength and extending to the tune-out wavelength. For a uniform power spectral density given by $PSD \approx 4 \cdot 10^{-17} \times P$, this would shift the measured value of the tune-out wavelength $+0.57$ fm.

Due to our uncertainty in the power spectral density near the tune-out wavelength, several tune-out wavelength measurements were also made using a 100 μm diameter pinhole. No shift in the measured values of the tune-out wavelength were observed for the measurements made using the larger pinhole.

3.2.3 Wavelength Measurement

Wavelength measurements were made using a Bristol Instruments model 621A wavemeter, which displays digits to 1 fm. The wavemeter is a source of both systematic and random

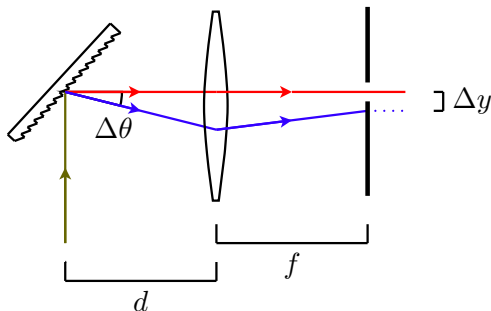


Figure 3.6: Schematic of spectral filtering optics.

errors in our measurement of the tune-out wavelength. We investigated the uncertainty of the wavemeter measurements by measuring four known alkali transitions in a saturated absorption experiment. The transitions used for this purpose include: ^{39}K D1 $F = 1 - F' = 2$ (crossover) $\rightarrow F' = 1 - F' = 2$ (crossover), ^{87}Rb D1 $F = 2 \rightarrow F' = 3$, ^{85}Rb D2 $F = 3 \rightarrow F' = 2$, and ^{133}Cs D2 $F = 3 \rightarrow F' = 4$. The result of the saturated absorption measurements are summarized in Table 3.1.

Transition	Known Wavelength (nm)	Measurement Error (fm)
^{39}K	770.108216	-32, -33
^{87}Rb	780.245945	-38, -44
^{85}Rb	794.982062	-25, -38
^{133}Cs	852.334606	-63, -78

Table 3.1: Result of saturation absorption measurements of known transitions in alkali atoms. Each transition was measured twice: once before our measurements of the tune-out wavelength, and a second time after the last tune-out wavelength measurement.

Using these results, we recalibrated the wavemeter readings near 790 nm. The difference between the wavemeter reading and the actual wavelength near 790 nm was found by fitting $\text{Error} = C(\lambda - 790 \text{ nm}) + \Delta$ to the error in the measured wavelengths versus the wavelength. Using a least-squares fit, we found that $\Delta = -39.7 \text{ fm} \pm 3.5 \text{ fm}$. This calibration offset was recalculated using various subsets of the four absorptions measurements. The average calibration offset was found to be $\Delta = -40 \text{ fm} \pm 5 \text{ fm}$. We treat Δ as a offset in our wavemeter calibration; we correct for this offset when recording our

measured wavelengths. The uncertainty in this offset represents systematic source of error in our wavelength measurements.

3.2.4 Vector Polarizability

In Section 1.2.2 it was shown that the polarizability may be decomposed into an irreducible representation of spherical tensors as

$$\alpha(\omega) = \alpha^{(0)}(\omega) + \mathcal{A} \cos \theta_k \frac{m_F}{F} \alpha^{(1)}(\omega) + \left(\frac{3 \cos^2 \phi - 1}{2} \right) \frac{3m_F^2 - F(F+1)}{F(2F-1)} \alpha^{(2)}(\omega) \quad (1.35)$$

where $\alpha^{(0)}(\omega)$, $\alpha^{(1)}(\omega)$, and $\alpha^{(2)}(\omega)$ are the scalar, vector, and tensor polarizabilities, respectively. For atoms uniformly distributed among the m_F states, $\langle \alpha(\omega) \rangle = \langle \alpha^{(0)}(\omega) \rangle$. For this reason we've chosen to measure the scalar polarizability.

Recall that the atoms in our experiment are pumped into the $|F = 2, m = 2\rangle$ state. As a result, the vector and tensor terms contribute to our measured polarizability in a way that depends on the polarization of the light as well as the orientation of the atomic quantization axis. In our experiment, we minimize the vector contribution, while the tensor component is measured and accounted for.

Vector contributions to the polarizability can be extremely large. For example, the vector contribution to the polarizability for σ^+ light ($\mathcal{A} = +1$ and $\theta_k = 0$) is large enough in $|F = 2, m = 2\rangle$ state to eliminate the tune-out wavelength between the $5P_{1/2}$ and $5P_{3/2}$ manifolds. This is easily understood as there are no $m = 3$ states in the $5P_{1/2}$ manifold.

For small vector contributions, the shift to the tune-out wavelength that arises as a result of the vector contribution may be approximated by linearizing $\alpha(\omega)$ about the tune-out wavelength of the scalar polarizability. Because the tensor polarizability is much smaller than the scalar polarizability, and because we are trying to minimize the vector

polarizability, we may approximate $d\alpha/d\lambda$ as $d\alpha^{(0)}/d\lambda$.

$$\begin{aligned}\alpha(\omega) &\approx \left. \frac{d\alpha^{(0)}}{d\lambda} \right|_{\lambda_0} (\lambda - \lambda_0) + \mathcal{A} \cos \theta_k \frac{m_F}{F} \alpha^{(1)} \Big|_{\lambda_0} \\ \lambda - \lambda_0 &\approx -\mathcal{A} \cos \theta_k \frac{m_F}{F} \frac{\alpha^{(1)} \Big|_{\lambda_0}}{\left. \frac{d\alpha^{(0)}}{d\lambda} \right|_{\lambda_0}}\end{aligned}\quad (3.10)$$

Because the polarizability is dominated by the coupling between our initial state $|F = 2, m = 2\rangle$ and the 5P manifold, we can estimate the values of $d\alpha^{(0)}/d\lambda$ and $\alpha^{(1)}$ by taking the sum only over the excited states in the 5P manifold in Eq. (1.39). For light near the tune-out wavelength of the scalar polarizability, we find that $d\alpha^{(0)}/d\lambda \approx 2517$ a.u./nm, and $\alpha^{(1)} \approx 12400$ a.u., resulting in $\frac{\alpha^{(1)}}{d\alpha^{(0)}/d\lambda} \approx 4.93$ nm. To measure the tune-out wavelength of the scalar polarizability to a precision of 10 fm, we must reduce $\mathcal{A} \cos \theta_k < 2(10^{-6})$. Two methods are used to minimize the vector contribution: linearly polarized light minimizes \mathcal{A} , while a rotating bias field reduces the time-average of $\cos \theta_k$.

Time-Average of The Vector Polarizability

Recall that atoms in the waveguide are held in place by a time-averaged potential created by three fields: a rotating bias field, given by Eq. (2.3); a linear quadrupole field which is phase locked to the rotation bias, given by Eq. (2.7); and a spherical quadrupole field which is generated by a pair of coils at opposite ends of the waveguide, given by Eq. (2.8).

$$\mathbf{B}_0 = B_0 (\hat{x} \cos(\Omega t) + \hat{z} \sin(\Omega t)) \quad (2.3)$$

$$\mathbf{B}_{lq} = B'_{lq} (x \hat{x} - z \hat{z}) \sin(\Omega t) \quad (2.7)$$

$$\mathbf{B}_y = B'_x (-x \hat{x} + 2y \hat{y} - z \hat{z}) \sin(\omega t) \quad (2.8)$$

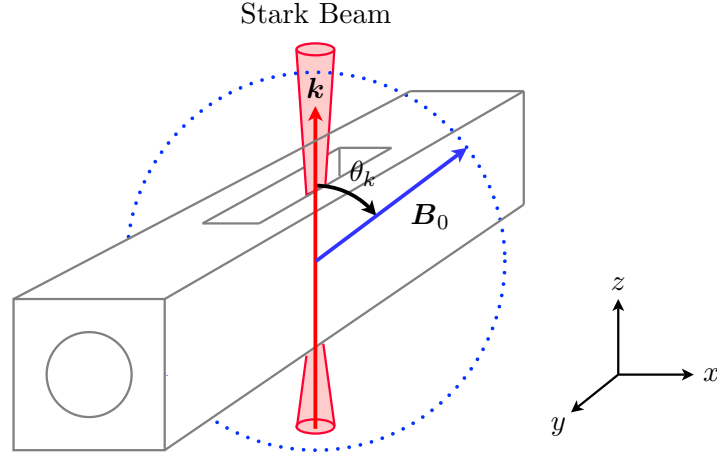


Figure 3.7: The figure above illustrates the orientation of the rotating bias field relative to the Stark beam in our experimental apparatus. The dotted line indicates the path traced out by the rotating bias. The block structure is the atom waveguide.

For a properly chosen linear quadrupole gradient (see Eq. (2.10)), the atoms are held in equilibrium at $\mathbf{r} = \langle 0, 0, 0 \rangle$, where the magnetic fields from both the linear quadrupole and the spherical quadrupole are zero.

Recall that, for atoms in the $|F = 2, m = 2\rangle$ state, the vector polarizability term is given by $\alpha(\omega)_{vec} = \mathcal{A} \cos \theta_k \alpha^{(1)}(\omega)$, where θ_k is the angle between the wave vector and the magnetic field. For atoms held in equilibrium, the rotating bias is the only magnetic field present. Because the light which imposes the Stark shift travels along the z-axis, while the rotating bias field rotates in the x-z plane, the angle θ_k rotates with the same frequency as the rotating bias, $\Omega = 2\pi \cdot 12.82$ kHz.

The atoms experience the Stark shift by traveling through a focused laser beam with a beam waist of $30 \mu\text{m}$. The atoms start $58.5 \mu\text{m}$ from center of the beam and travel for 10 ms at a speed of $v = 11.7$ mm/s to a point equidistant from, and on the opposite side of, the Stark beam. The atoms are then reflected, and travel for 10 ms back to their initial position. The rotating bias undergoes 256.4 rotations during this time. Because the intensity of the light seen by the atoms changes as the atoms move through the Stark

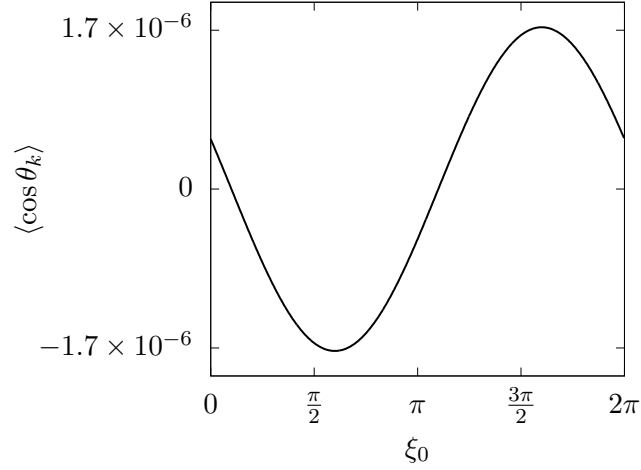


Figure 3.8: The vector polarizability time average dependence on the initial phase ξ_0 .

beam, we look at the time-average of $\cos \theta_k$ weighted by $I(t)$.

$$\langle \cos \theta_k \rangle = \frac{\int_0^{t_f} \cos(\Omega t + \xi_0) I(t) dt}{\int_0^{t_f} I(t) dt} \quad (3.11)$$

where ξ_0 describes the initial orientation of the rotating bias field.

For the tune-out wavelength measurement discussed here $I(t)$ is given by

$$I(t) = I_0 e^{\frac{-2(|v t - 2 x_0| - x_0)^2}{w^2}} \quad (3.12)$$

where $I_0 = 12.7 \text{ W/mm}^2$; x_0 , v , and w are the initial position of the atoms, their velocity, and the beam waist respectively.

Plugging Eq. (3.12) into Eq. (3.11) and factoring out the ξ_0 dependence gives

$$\langle \cos \theta_k \rangle = \cos \left(\frac{2\Omega x_0}{v} + \xi_0 \right) \frac{\int_0^{t_f} \cos \left(\frac{\Omega x_0}{v} + t \right) I(t) dt}{\int_0^{t_f} I(t) dt} \quad (3.13)$$

Numerically integrating Eq. (3.13) reveals that $\langle \cos \theta_k \rangle$ achieves a maximum value of $1.7 (10^{-6})$ when $\xi_0 = -\frac{2\Omega x_0}{v}$.

Field imperfections, such as a dc background field or the atoms being displaced from

the quadrupole zero, will increase the value of $\langle \cos \theta_k \rangle$. For the tune-out wavelength measurements discussed here, the phase of the rotating bias was synced to the experiment. To verify that the time-averaging adequately reduced vector polarizability contribution, several measurements were made using different values of ξ_0 . No shift in our measured values of the tune-out wavelength were observed for these measurements.

Linearizing Polarization of the Stark Beam

The vector polarizability is further reduced through the use of a linearly polarized Stark beam. A calcite polarizer is used to establish the initial polarization of the light. However, before reaching the atoms, the Stark beam interacts with various optics which alter the light's polarization. A zeroth-order quarter-wave plate is placed between the calcite polarizer and the atoms to correct for the ellipticity caused by the optics.

One major challenge with linearizing the polarization of the light, is accounting for the birefringence of the vacuum chamber in which the experiment was conducted. To address this issue, an interferometry measurement was designed to be sensitive to the vector polarizability, while minimizing our sensitivity to the scalar polarizability. The vector polarizability interferometer is essentially the same as the interferometer used to measure the scalar polarizability. Because $\alpha(\omega)_{vec}$ is proportional to \mathcal{A} , measuring the vector polarizability effectively measures the polarization of the light that interacts with the atoms.

To maximize the interferometer's sensitivity to the vector polarizability, the Stark beam was pulsed in sync with the rotating bias field, so that the Stark beam is only applied when $\cos \theta_k$ is positive. As a result, the time-average of $\cos \theta_k$ was increased from $1.7(10^{-6})$ to $2/\pi$. To minimize the interferometer's sensitivity to the scalar polarizability, the wavelength of the Stark beam was set close to the tune-out wavelength for the scalar polarizability. For light that is 1 pm detuned from the tune-out wavelength of the scalar polarizability, $\alpha^{(1)}$ is nearly 50,000 times larger than $\alpha^{(0)}$. Due to the relative strengths

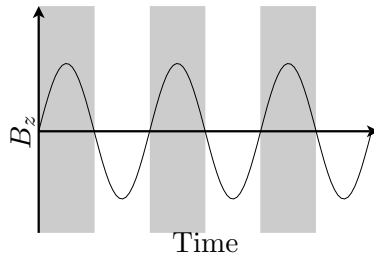


Figure 3.9: Stark beam timing for the vector polarizability measurement.

of the scalar and vector polarizabilities, we did not need to know the exact value of the tune-out wavelength for the vector polarizability measurements.

To verify the interferometer measurements were sensitive to the vector polarizability, two separate measurements were made: one measurement was made by applying the Stark beam only when $\cos \theta_k$ was positive, a second measurement was made by applying the Stark beam only when $\cos \theta_k$ was negative. Because $\alpha(\omega)_{vec}$ is proportional to $\cos \theta_k$, changing the timing of the Stark beam pulses in this way should change the sign of the phase shift caused by the vector polarizability. The scalar polarizability is not affected by the direction of the magnetic field. As a result, the phase shift caused by the scalar polarizability should have the same sign for both types of measurements. Both types of measurements were used when linearizing the polarization of the Stark beam.

Our tune-out wavelength measurement's sensitivity to the polarization of the Stark beam was empirically measured. We found that a 1° rotation of the quarter-wave plate in the Stark beam's path shifted the measured tune-out wavelength by about 360 fm. This suggests our time-average of $\cos \theta_k$ is $4(10^{-3})$, more than 2000 times larger than the idealized time-average calculated from Eq. (3.13). This discrepancy is likely the result of an environmental magnetic field, which biases the time-averaging.

The initial linearization of the Stark beam's polarization was limited by our ability to adjust the quarter-wave plate. For each tune-out wavelength measurement, the quarter-wave plate was adjusted to within 0.1° of the desired orientation, resulting in $\mathcal{A} \approx 2(10^{-3})$. However, each tune-out wavelength measurement took several hours to complete and,

during this time, the polarization of Stark beam drifted. We account for this drift by measuring the polarization of the Stark beam at the end of each tune-out wavelength measurement. We used our empirically measured polarization sensitivity to estimate the error that resulted from this polarization.

3.2.5 Tensor Polarizability

While significantly smaller, the tensor polarizability also contributes to the measured tune-out wavelength. We determine the tune-out wavelength of the scalar polarizability by measuring and accounting for the shifts in the tune-out wavelength caused by contributions from the tensor polarizability. We identify the tensor contributions through their dependence on the angle between the polarization of the linearly polarized Stark shifting light and the rotating bias field, θ_p . To measure these tensor contributions, tune-out wavelength measurements were made for several values of θ_p . A half-wave plate was used to adjust the polarization of the Stark shifting light.

For linearly polarized light incident on atoms in the $|F = 2, m_F = 2\rangle$ state, the vector contribution vanishes and Eq. (1.35) reduces to [23, 24, 25]

$$\begin{aligned}\alpha(\omega) &= \alpha^{(0)}(\omega) + \left(\frac{3}{4} \cos^2 \theta_p - \frac{1}{2}\right) \frac{3m_F^2 - F(F+1)}{F(2F-1)} \alpha^{(2)}(\omega) \\ \alpha(\omega) &= \alpha^{(0)}(\omega) + \left(\frac{3}{4} \cos^2 \theta_p - \frac{1}{2}\right) \alpha^{(2)}(\omega)\end{aligned}\tag{3.14}$$

Where θ_p is the angle between the polarization of the light and external magnetic field. Note that, due to time-averaging of the rotating bias field, an additional factor of $1/2$ appears in front of the $\cos^2 \theta_p$ term.

The shift to the tune-out wavelength that arises as a result of the tensor contribution may be approximated by linearizing $\alpha(\omega)$ about the tune-out wavelength of the scalar polarizability. Because $\alpha^{(2)}(\omega)$ is much smaller than $\alpha^{(0)}(\omega)$, we may approximate $d\alpha/d\lambda$

as $d\alpha^{(0)}/d\lambda$.

$$\begin{aligned}\alpha(\omega) &\approx \left. \frac{d\alpha^{(0)}}{d\lambda} \right|_{\lambda_0} (\lambda - \lambda_0) + \left(\frac{3}{4} \cos^2 \theta_p - \frac{1}{2} \right) \alpha^{(2)} \Big|_{\lambda_0} \\ \lambda - \lambda_0 &\approx - \left(\frac{3}{4} \cos^2 \theta_p - \frac{1}{2} \right) \frac{\alpha^{(2)} \Big|_{\lambda_0}}{\left. \frac{d\alpha^{(0)}}{d\lambda} \right|_{\lambda_0}}\end{aligned}\quad (3.15)$$

Once again we may estimate the values of $\frac{d\alpha^{(0)}}{d\lambda}$ and $\alpha^{(2)}$ by using Eq. (1.39) and taking the sum over the excited states in the 5P manifold. For light near the tune-out wavelength $\alpha^{(2)} = 2.010 (10^{-25}) \text{ cm}^3$, and $\frac{d\alpha^{(0)}}{d\lambda} \approx 3.735 (10^{-22}) \text{ cm}^3/\text{nm}$. This results in $\frac{\alpha^{(2)}}{d\alpha^{(0)}/d\lambda} = 538.2(4) \text{ fm}$. Looking at Eq. (3.15) we see that the tensor contribution both shifts the tune-out wavelength by +270 fm and adds a measurable oscillation with an amplitude of 202 fm. Note that, because the tensor contribution shifts the tune-out wavelength by $\frac{1}{2} \left(\frac{\alpha^{(2)}}{d\alpha^{(0)}/d\lambda} \right)$ regardless of the orientation of the Stark light polarization, our measurement of the tune-out wavelength for the scalar polarizability is sensitive to the value of $\frac{\alpha^{(2)}}{d\alpha^{(0)}/d\lambda}$.

Chapter 4

Results

4.1 Results of The Tune-out Wavelength Measurement

Our reported value of the tune-out wavelength was determined through 21 tune-out wavelength measurements. Measurements were made at five polarization angles θ_p . As outlined in Section 3.2.5, we used the tensor polarizability's dependence on the polarization angle θ_p to account for the shifts in the tune-out wavelength caused by tensor contributions. We determined the tune-out wavelength of the scalar polarizability by plotting our tune-out wavelength measurements against the polarization angle θ_p and fitting the data to Eq. (3.15). Because multiple tune-out wavelength measurements were made at each angle θ_p , these measurements were combined through an average which was weighted by the uncertainty in each measurement. The uncertainty in each tune-out wavelength measurement was found by combining the statistical uncertainty in the linear fit, described in Section 3.1, with the estimated error caused by polarization drift, described in Section 3.2.4. The uncertainty of the weighted average was calculated according to the formula $\sigma^2 = 1/\sum_i \sigma_i^{-2}$.

Fitting the averaged tune-out wavelength measurements to Eq. (3.15), while using both $\frac{\alpha^{(2)}}{d\alpha^{(0)}/d\lambda}$ and λ_0 as fitting parameters, gives $\frac{\alpha^{(2)}}{d\alpha^{(0)}/d\lambda} = 390(120)$ fm and $\lambda_0 =$

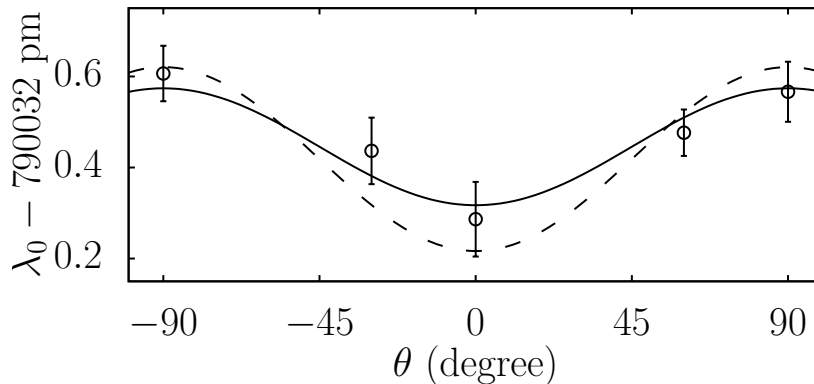


Figure 4.1: Tune-out wavelength measurements for light linearly polarized an angle θ from the x-axis.

790.032377(35) nm. The fit, which has a $\chi^2/\text{d.o.f.}$ of 0.5, is shown as the solid curve in Fig. 4.1. In Section 3.2.5, the value of $\frac{\alpha^{(2)}}{\text{d}\alpha^{(0)}/\text{d}\lambda}$ was calculated using Eq. (1.39). From this calculation we found $\frac{\alpha^{(2)}}{\text{d}\alpha^{(0)}/\text{d}\lambda} = 538.2(4)$ fm, which is about 1.3σ larger than the value obtained from the fit. Performing a fit in which the value of $\frac{\alpha^{(2)}}{\text{d}\alpha^{(0)}/\text{d}\lambda}$ is constrained to the calculated value of 538.2 fm, we find that $\lambda_0 = 790.032326(29)$ nm, which is about 1σ smaller than the value obtained from the unconstrained fit. The constrained fit has a $\chi^2/\text{d.o.f.}$ of 1.2, and is shown as the dashed curve in Fig. 4.1. Because the calculated value of $\frac{\alpha^{(2)}}{\text{d}\alpha^{(0)}/\text{d}\lambda}$ is expected to be accurate, we report the value obtained using the constrained fit.

4.2 Error Analysis

As outlined in Section 3.1, each tune-out wavelength measurement was made by interpolating a set of dynamic polarizability measurements made at various wavelengths to find the wavelength at which $\alpha(\omega) = 0$. This interpolation was accomplished through a linear fit of the polarizability measurements versus the wavelength. Estimated errors in the polarizability measurements and the wavelengths at which these measurements were

made were included in the linear fit. The statistical error in the tune-out wavelength measurement is derived from the uncertainty in this fit. The average statistical error in the tune-out wavelength measurement was 60 fm.

The statistical error in each tune-out wavelength measurement incorporates estimated errors in the polarizability measurements. The polarizability was determined by measuring the slope of the phase that accumulates when an atom packet passes through the Stark beam versus the overall power in the beam. The linear fit used to determine this slope provides a statistical error, which is used as the estimated error for the polarizability measurement. The wavelength of the Stark beam was measured periodically during the polarizability measurement; the standard deviation of the measured wavelengths was used to estimate the error in the wavelength at which the polarizability was measured.

Because we seek to measure the tune-out wavelength of the scalar polarizability, contributions from the vector polarizability constitute a significant source of error. As outlined in Section 3.2.4, vector polarizability contributions were minimized by using a linearly polarized Stark beam. However, polarization drifts, which occur over the course of each tune-out wavelength measurement, result in slight deviations from linear polarization. To estimate the error arising from these polarization drifts, measurements of the polarization were made at the start and end of each tune-out wavelength measurement. Because each tune-out wavelength measurement occurs over the course of several hours, we are not confident that the polarization drift is linear, or even monotonic. As a result, we use the full value of the polarization drift to estimate the error. The resulting error in the tune-out wavelength measurement was determined through an empirical calibration, which determined the sensitivity of our tune-out wavelength measurement to the polarization of the Stark beam. The average error in the tune-out wavelength measurements caused by polarization drift is 126 fm.

Averaging the 21 tune-out wavelength measurements reduces the estimated error in the tune-out wavelength by a factor of $\sqrt{20}$, resulting in statistical and polarization drift er-

rors of 13 fm and 28 fm, respectively. Statistical and polarization errors vary considerably between tune-out wavelength measurements. As noted in Section 3.2.5, when calculating the tensor contribution to the tune-out wavelength, the measurements from each polarization angle were combined using a weighted average given by $\sum_i w_i x_i / w_i$ where the weight w_i is given by $w_i = 1/\sigma_i^2$ and σ_i is the combined statistical and polarization error. The uncertainty in the weighted average is given by $\sigma^2 = 1/\sum_i \sigma_i^{-2}$. The tensor polarizability fit, described in Section 3.2.5, was used to determine the tune-out wavelength of the scalar polarizability. The fit provided an error for the tune-out wavelength which effectively combines the statistical and polarization drift errors of all the measurements. This combined error is 32 fm.

The wavelength measurements also contributed to the error in the tune-out wavelength. As outlined in Section 3.2.3, we used a Bristol Instruments model 621A wavemeter which was calibrated using known saturation absorption lines in K, Rb, and Cs. The calibration indicated that a correction of $\Delta = -40 \text{ fm} \pm 5 \text{ fm}$ should be applied to the measured wavelength. The uncertainty in the calibration presents a systematic error in our wavelength measurements. The wavemeter was calibrated before and after the full run of tune-out wavelength measurements.

As discussed in Section 3.2.2, another significant source of error comes from the broadband light in the Stark beam. To reduce this effect, the Stark beam was spectrally filtered through a 0.34 nm band-pass filter using a diffraction grating and pinhole. While the power spectral density near 780 nm was determined via scattering rate measurements, the power spectral density may vary significantly between 780 and 790 nm. Because of the difficulty in measuring low spectral power levels near the lasing wavelength of 790 nm, we quantified the effect of broadband light on our tune-out wavelength measurements by comparing the measurements made using 0.17 nm and 0.34 nm band-pass filters. Approximately half of the measurements were made using each filter. No measurable difference was observed, within our 30 fm precision. Since the error resulting broadband light is expected to scale

with the bandwidth squared, the agreement between our two sets of measurements suggests an error of less than 10 fm for the smaller bandwidth configuration. We report the estimated error from broadband light as 10 fm.

Uncertainty in the waveguide magnetic field introduces an additional source of error through its effect on the $\langle \cos^2 \theta_p \rangle$ term, which factors into the tensor polarizability as shown in Eq. (3.2.5). This has the potential to shift the measured tune-out wavelength by altering the value of the fitting parameter λ_0 in Eq. (3.15). The effect of a particular defect may be found by calculating the change to Eq. (3.15) caused by a non-ideal magnetic field in which $\langle \cos^2 \theta_p \rangle \neq 1/2 \cos^2 \theta_p$.

$$\Delta\lambda_0 \approx - \left(\frac{3}{4} \cos^2 \theta_p - \frac{3}{2} \langle \cos^2 \theta_p \rangle \right) \frac{\alpha^{(2)}|_{\lambda_0}}{\frac{d\alpha^{(0)}}{d\lambda}|_{\lambda_0}} \quad (4.1)$$

Note that the equation above gives the shift in the tune-out wavelength at a particular polarization angle θ_p . Of particular importance are effects which shift the tune-out wavelength when averaged over all polarization angles θ_p , as this will shift the value of the fitting parameter λ_0 . As a result, the shift in the fitting parameter λ_0 is found by averaging Eq. (4.1) over all possible angles θ_p .

The most significant shift to the tune-out wavelength appears to occur when a time-dependent bias field is applied along the z direction. We are able to place a limit on the strength of such a field by measuring the Zeeman linewidth of trapped atoms using rf spectroscopy. These measurements suggest that the magnitude of the Bias varies by less than 2%, which, in the worst case, would result in a 1.0 fm shift to the tune-out wavelength. Other effects are smaller. For example, a 1 G dc background field pointing perpendicular to the plane of the rotating bias, would shift in the tune-out wavelength approximately 0.5 fm. We estimate the error arising from all field defects to be 2 fm.

Hyperpolarizability creates an additional source of error. As outlined in Section 1.2.3, at peak intensity and at 790 nm, the hyperpolarizability contributes approximately

Source	Error (fm)
Statistical	13
Polarization drift	28
Stat. and polz. combined	29
Broadband spectrum	10
Wavemeter calibration	5
Field defects	2
Hyperpolarizability	1
Total	31

Table 4.1: Tune-out wavelength error estimates. The entries for statistical error and polarization drift report the average errors for each type divided by the square root of the number of measurements. In the analysis, both errors were combined at each data point to give the reported combined error in the result.

$9.6 (10^{-4})$ a.u. to the polarizability, shifting the tune-out wavelength by 0.3 fm. We approximate the error to the tune-out wavelength from hyperpolarizability to be 1 fm.

As outlined in Section 3.2.4, atoms held in the equilibrium of the magnetic waveguide potential experience a rotating bias field. This magnetic field results in Zeeman shifts, which alter the measured value of the tune-out wavelength. Using rf spectroscopy, the magnitude of the rotating bias field was measured to be 20.0(2) G. We estimate the change in the tune-out wavelength caused by the Zeeman shifts by calculating the tune-out wavelength with and without adjusting the resonances to account for the Zeeman shifts. From these calculations we found that the Zeeman shift moves the tune-out wavelength by +26 fm. The value of the tune-out wavelength reported here and in Section 4.1 was corrected to give the value of the tune-out wavelength in the absence of magnetic fields. We estimate the error in this correction to be less than 1 fm.

4.3 Comparison to Theory

No other experimental measurements exist for Rb in the $F = 2$ hyperfine ground state. However, we can make a useful comparison to theory.

For alkali atoms, the polarizability is dominated by the coupling of the valence electron to the first few excited states. Because of this, it is convenient to separate contributions from the valence electron from the contributions of core electrons and core-valence interactions. In Eq. (1.32) we denote these core and core-valence contributions as α_{other} . α_{other} is approximately static and may be calculated in the random phase approximation [31]. The value of α_{other} used here was calculated by M. S. Safronova. The valence contributions to the polarizability, given by Eq. (1.33), may be rewritten in terms of atomic units as

$$\alpha^v(\omega) = \frac{1}{3} \sum_k \frac{\langle k || d || 5S \rangle^2 (E_k - E_{5S})}{(E_k - E_{5S})^2 - E_L^2} \quad (4.2)$$

where $k = nP_{1/2}$ and $nP_{3/2}$, and E_L is the energy carried by a photon measured in atomic units.

Each term in the sum is evaluated up to $n = 12$ using the experimental values for the transition energies $E_k - E_{5S}$. Experimental values from [32] are used for the $5S - 6P$ transitions while all other matrix elements use the all-order calculations found in [31]. The details of the methods are discussed in [33]. While experimental values are available for the $5S - 5P$ matrix elements [34], the theoretical values are estimated to have a more accurate ratio, which is more important for tune-out wavelength calculations. Contributions for $n > 12$ are calculated by M. S. Safronova in Ref. [35] using the Dirac-Hartree-Fock approximation.

Because the tune-out wavelength was measured for Rb atoms in a particular hyperfine state, hyperfine structure must be included in the theoretical determination of the tune-out wavelength. Due to the larger dipole matrix elements and smaller detuning for the $5P$ transitions, the effect of hyperfine structure is negligible for all but the $5P$ transitions. The hyperfine dependence of the dipole matrix elements may be written in terms the reduced

matrix elements $\langle J||d||J' \rangle$ as

$$\langle 5S_{1/2}, F = 2 || d || 5P_{J'}, F' \rangle = -1^{F'+J+I+1} \sqrt{(2F+1)(2F'+1)} \begin{Bmatrix} 1/2 & J' & 1 \\ F' & 2 & 3/2 \end{Bmatrix} \quad (4.3)$$

The hyperfine dipole matrix elements for $5P$ hyperfine transitions are calculated using the theoretically calculated values of $\langle 5S || d || 5P_{1/2} \rangle = 4.2199 ea_0$ and $\langle 5S || d || 5P_{3/2} \rangle = 5.9550 ea_0$ as described above.

Using these values, the tune-out wavelength is calculated to be $\lambda_0 = 790.03108$ nm. The individual contributions to the polarizability at $\lambda = 790.03108$ nm are shown in Table 4.2 along with the transition energies $\Delta E = E_k - E_{5S}$ and dipole matrix elements.

4.3.1 Uncertainty in Theoretical Tune-Out Wavelength Prediction

Uncertainty in the theoretically calculated tune-out wavelength is dominated by our uncertainty in the $5P$ dipole matrix elements. We estimate the uncertainty in the calculated tune-out wavelength by comparing the results of tune-out wavelength calculations performed using various values of the $5P$ dipole matrix elements. The values of the $5S - 5P$ matrix elements were calculated in [31] using the following theoretical methods: lowest-order Dirac-Hartree-Fock (DF), second and third-order many-body perturbation theory (II and III), *ab initio* all-order calculations in the single-double approximation (SD) with inclusion of the partial triple contributions (SDpT), as well as scaled all-order calculations (SD_{sc}, SDpT_{sc}). The values of the $5P$ dipole matrix elements, along with the values of the tune-out wavelength calculated using the dipole values are shown in Table 4.3. The tune-out wavelengths calculated in Table 4.3 differ only in the values of the two $5P$ matrix elements, with all other values taken from Table 4.2.

The most accurate methods are expected to be the four all-order calculations: SD, SDpT, SD_{sc}, and the SDpT_{sc}. We take the average of these four values as the final

Contribution	ΔE	d	α_0
$5P_{1/2}, F' = 1$	0.57313455	4.7180	-4115.986
$5P_{1/2}, F' = 2$	0.57313579	4.7180	-4117.408
$5P_{1/2}$			-8233.394
$6P_{1/2}$	0.1080539	0.3235(9)	0.452(2)
$7P_{1/2}$	0.126826	0.115(3)	0.044(2)
$8P_{1/2}$	0.135938	0.060(2)	0.011(1)
$9P_{1/2}$	0.141059	0.037(3)	0.004(1)
$10P_{1/2}$	0.144226	0.026(2)	0.002
$11P_{1/2}$	0.14632	0.20(1)	0.001
$12P_{1/2}$	0.147778	0.016(1)	0.001
$(n > 12)P_{1/2}$			0.022(22)
$5P_{3/2}, F' = 1$	0.58396076	2.1054	411.164
$5P_{3/2}, F' = 2$	0.58396099	4.7078	2055.752
$5P_{3/2}, F' = 3$	0.58396140	7.8777	5755.784
$5P_{3/2}$			8222.7
$6P_{3/2}$	0.108407	0.5230(8)	1.173(4)
$7P_{3/2}$	0.126986	0.202(4)	0.135(6)
$8P_{3/2}$	0.136024	0.111(3)	0.037(2)
$9P_{3/2}$	0.141111	0.073(5)	0.015(2)
$10P_{3/2}$	0.144259	0.053(4)	0.008(1)
$11P_{3/2}$	0.146343	0.040(3)	0.004(1)
$12P_{3/2}$	0.147794	0.033(2)	0.003
$(n > 12)P_{3/2}$			0.075(75)
Other			8.709(93)
Total			0.002

Table 4.2: Breakdown of the contributions to the $5S$ polarizability in Rb at $\lambda_0 = 790.03108$ nm. The transition energies ΔE , reduced matrix elements d , and polarizability contributions are given in atomic units. Experimental matrix elements from Ref. [32] are used for the $5S - 5P$ transitions; remaining matrix elements are from all-order calculations [31]. Uncertainties are given in parenthesis.

theoretical prediction for the tune-out wavelength and use the full spread of these values to estimate the error resulting from our uncertainty in values of the $5S - 5P$ dipole matrix elements. This gives a final theoretical value of $\lambda_0 = 790.0315(7)$ nm. This differs from the measured value by 1.2σ , with the theoretical uncertainty about twenty times larger than the experimental uncertainty.

We may estimate the non- $5P$ contributions to the uncertainty in the theoretical value of the tune-out wavelength by calculating the uncertainty in the α contributions from all other sources at the tune-out wavelength, we then relate this to the derivative $\frac{d\alpha}{d\lambda}$ to determine the resulting uncertainty in λ_0 . The uncertainties in the α contributions listed in Table 4.2 arise from uncertainties in the dipole matrix elements, and may be calculated using propagation the errors. The combined the uncertainty in α from all non- $5P$ contributions at the tune-out wavelength is 0.009 a.u. The derivative $\frac{d\alpha}{d\lambda} \approx 2.5 \frac{\text{a.u.}}{\text{pm}}$ near the tune-out wavelength, suggesting a 3.6 fm wavelength error arising from uncertainties in all non- $5P$ contributions.

While the uncertainties from non- $5P$ sources contribute negligibly to the uncertainty in theoretical value of the tune-out wavelength, non- $5P$ contributions do contribute significantly to the theoretical value of the tune-out wavelength. From Table 4.2 we see that at the theoretically calculated tune-out wavelength non- $5P$ contributions to α total to 10.67 a.u., shifting the theoretical value of the tune-out wavelength by -4.27 pm.

As noted above contributions from the $5P$ transitions dominate theoretical calculations of the tune-out wavelength. Because the two $5P$ transitions contribute to the polarizability with opposite sign, the theoretical calculation is particularly sensitive to the ratio of the two $5P$ dipole matrix elements.

$$R = \frac{|\langle 5P_{3/2} || d || 5S \rangle|^2}{|\langle 5P_{1/2} || d || 5S \rangle|^2} \quad (4.4)$$

This is convenient, because the theoretical accuracy of the ratio is better than the the-

	DF	II	III	SD	SD _{sc}	SDpT	SDpT _{sc}
$5S - 5P_{1/2}$	4.8189	4.5981	4.1855	4.2199	4.2535	4.2652	4.2498
$5S - 5P_{3/2}$	6.8017	6.4952	5.9047	5.9550	6.0031	6.0196	5.9976
λ_0 (nm)	790.03145	790.03698	790.02920	790.03108	790.03177	790.03173	790.03147
R	1.9922	1.9954	1.9902	1.9914	1.9919	1.9918	1.9917

Table 4.3: Values of the reduced dipole matrix elements for the $5S - 5P$ transitions calculated using various theoretical methods, along with the dipole ratio R and the resulting theoretical value of the tune-out wavelength λ_0 . The values of the $5S - 5P$ matrix elements were calculated in [31] using the following theoretical methods: lowest-order Dirac-Hartree-Fock (DF), second and third-order many-body perturbation theory (II and III), *ab initio* all-order calculations in the single-double approximation (SD) with inclusion of the partial triple contributions (SDpT), as well as scaled all-order calculations (SD_{sc}, SDpT_{sc}).

oretical accuracy of the individual matrix elements as a large fraction of the correlation corrections cancel. This can be seen in Table 4.3, where the value of $\langle 5P_{3/2} || d || 5S \rangle$, $\langle 5P_{1/2} || d || 5S \rangle$, and R are calculated using various theoretical methods. Using the measured tune-out wavelength as an input, we can use the equations we used to calculate the theoretical value of the tune-out wavelength (Eqs. 1.32 and 4.2) to make an experimental determination of the dipole ratio R . For this calculation we use the average of several experimental measurements of $\langle 5S || d || 5P_{1/2} \rangle = 4.233(2) ea_0$ [34, 36, 37], while using Eq. 4.3.1 to express $\langle 5S || d || 5P_{3/2} \rangle$ in terms of the dipole ratio R . Setting the wavelength equal to the experimentally determined tune-out wavelength $\lambda = 790.032326$ nm, and solving for the value of R at which $\alpha = 0$, gives $R = 1.99217(3)$, where the uncertainty in R is calculated by propagation of errors.

Chapter 5

Outlook

5.1 Future Tune-out Wavelength Measurements

Using the same technique outlined in this thesis, further tune-out wavelength measurements may be performed in ^{87}Rb . Of particular interest is the tune-out wavelength between the $5P$ and $6P$ manifolds, as well as the tune-out wavelength between the $6P_{1/2}$ and $6P_{3/2}$ states. The individual contributions to the polarizability at both tune-out wavelengths are shown in Table 5.1.

As shown in Table 5.1, the tune-out wavelengths near 421 nm and 423 nm are determined largely through the contributions of the $5P_{1/2}$, $5P_{3/2}$, $6P_{1/2}$, and $6P_{3/2}$ states. Moreover, the contributions to the polarizability from these states are comparable in magnitude. In comparison, the tune-out wavelength near 790 nm is determined almost entirely by the cancellation of contributions from the $5P_{1/2}$ and $5P_{3/2}$ states. In Section 4.3.1, this was used to determine the dipole ratio $R = |\langle 5P_{3/2} || d || 5S \rangle|^2 / |\langle 5P_{1/2} || d || 5S \rangle|^2$. In a similar manner, measurements of the tune-out wavelength at both 421 nm and 423 nm may be combined with the measured dipole ratio R to determine the electric dipole matrix elements $\langle 6P_{1/2} || d || 5S \rangle$ and $\langle 6P_{3/2} || d || 5S \rangle$.

The largest sources of error in the 790 nm tune-out wavelength measurement were

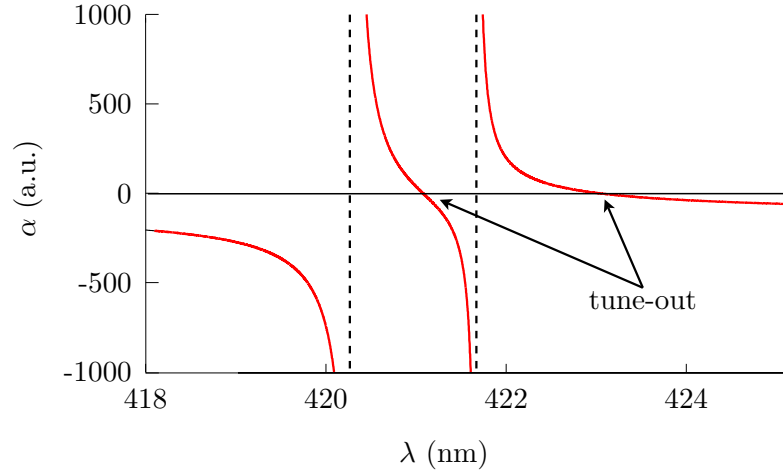


Figure 5.1: Tune-out wavelengths near 420 nm in Rb.

Contribution	$\alpha_0(421.08 \text{ nm})$	$\alpha_0(423.03 \text{ nm})$
$5P_{1/2}$	-40.386	-40.910
$6P_{1/2}$	-113.875	50.423
$7P_{1/2}$	0.128	0.125
$8P_{1/2}$	0.024	0.024
$9P_{1/2}$	0.008	0.008
$10P_{1/2}$	0.004	0.004
$11P_{1/2}$	0.002	0.002
$12P_{1/2}$	0.001	0.001
$5P_{3/2}$	-83.181	-84.276
$6P_{3/2}$	228.035	65.371
$7P_{3/2}$	0.391	0.382
$8P_{3/2}$	0.082	0.081
$9P_{3/2}$	0.031	0.030
$10P_{3/2}$	0.015	0.015
$11P_{3/2}$	0.008	0.008
$12P_{3/2}$	0.005	0.005
Other	8.709(93)	8.709(93)
Total	0.001	0.002

Table 5.1

statistical errors and contributions from the vector polarizability. As detailed in Section 3.2.4, vector polarizability contributions shift the tune-out wavelength by an amount that depends on the vector polarizability term $\alpha^{(1)}$ and the slope $d\alpha/d\lambda$.

$$\lambda - \lambda_0 \approx -\mathcal{A} \cos \theta_k \frac{m_F}{F} \frac{\alpha^{(1)} \Big|_{\lambda_0}}{\frac{d\alpha^{(0)}}{d\lambda} \Big|_{\lambda_0}} \quad (3.10)$$

At both of the 420 nm tune-out wavelengths, the vector polarizability terms $\alpha^{(1)}$ are significantly smaller: -227 a.u. and $+18$ a.u. at 421 nm and 423 nm, respectively, compared to $\alpha^{(1)} = 1200$ a.u. at 790 nm. However, the value of the slope $d\alpha/d\lambda$ is also smaller: -0.51 a.u./pm and 0.90 a.u./pm at 421 nm and 423 nm, respectively, compared to 2.5 a.u./pm at 790 nm. Taken together, the tune-out wavelength measurements near 420 nm will be significantly less sensitive to contributions from the vector polarizability, with the ratio $\frac{\alpha^{(1)}}{d\alpha/d\lambda}$ equal to 446 pm and 20.1 pm at 421 nm and 423 nm, compared to 4942 pm at 790 nm.

However, due to the smaller value of $d\alpha/d\lambda$, the interferometer will be less sensitive to wavelength near the two 420 nm tune-out wavelengths. This loss of sensitivity will likely result in a larger statistical error. The sensitivity of the interferometer may be recovered through the use of higher intensity Stark light. The intensity of the Stark beam is limited by two factors: scattering rate and hyperpolarizability. The scattering rate is given by

$$R_s = \frac{\Gamma}{2} \left(\frac{\frac{I}{I_{\text{sat}}}}{1 + \frac{I}{I_{\text{sat}}} + 4 \left(\frac{2\pi\Delta}{\Gamma} \right)^2} \right) \quad (5.1)$$

The linewidths for the $6P_{1/2}$ and $6P_{3/2}$ states are $2\pi \cdot 1.27$ MHz and $2\pi \cdot 1.42$ MHz[31], respectively. While the saturation intensities may be calculated using[38]

$$I_{\text{sat}} = \frac{c\epsilon_0\Gamma^2\hbar^2}{4|\hat{\epsilon} \cdot \mathbf{d}|^2} \quad (5.1)$$

where $\hat{\epsilon}$ is the normalized polarization vector. The saturation intensities for the $6P_{1/2}$ and $6P_{3/2}$ states are 6.28 mW/cm^2 and 2.99 mW/cm^2 , respectively. The scattering rate is largest at the 421 nm tune-out wavelength. For light at 421 nm with a beam waist of $30 \mu\text{m}$, the scattering rate is related to the total power in the Stark beam by $R_s \approx P(\text{mW}) \times 0.05 \text{ Hz}$, at peak intensity. From these numbers we find that approximately 10% of the atoms will be scattered when exposed to a 110 mW Stark beam for 20 ms.

In Section 1.2.3 we found that the hyperpolarizability contribution to the polarizability is given by

$$\Delta\alpha(\omega) \approx -\frac{1}{8}\gamma_n(\omega)\frac{I}{c\epsilon_0} \quad (1.42)$$

Summing over the $6P_{1/2}$ and $6P_{3/2}$ states in Eq. 1.42 gives $\Delta\alpha \approx 1.8(10^{-13}) \frac{\text{a.u.}}{\text{W/m}^2}$ and $\Delta\alpha \approx 1.4(10^{-14}) \frac{\text{a.u.}}{\text{W/m}^2}$ at 421 nm and 423 nm, respectively. We can relate the shift to the polarizability to a shift in the tune-out wavelength through the derivative $d\alpha/d\lambda$. The shift to the tune-out wavelength caused by hyperpolarizability contributions is largest for the 421 nm tune-out wavelength. For light at 421 nm with a beam waist of $30 \mu\text{m}$, the hyperpolarizability shifts the tune-out wavelength by $\Delta\lambda \approx P(\text{mW}) \times 2.5(10^{-4}) \text{ fm}$, suggesting that hyperpolarizability will not play a role in limiting the power of the Stark beam.

Appendices

Appendix A

AOM Configuration

Light used in the saturated absorption measurements, which were used to calibrate the wavemeter, passes through several acousto-optical modulators (AOM). As a result, the wavelength of the light sent to the atoms is shifted -18.6 MHz relative to the wavelength measured by the wavemeter. Values reported in Section 3.2.3 account for this shift.

Similarly, the light sent to the atoms for the tune-out wavelength measurement passes through an AOM, which shifts the wavelength relative to the wavelength sent to the wavemeter. The tune-out wavelengths reported in this thesis account for this shift as well.

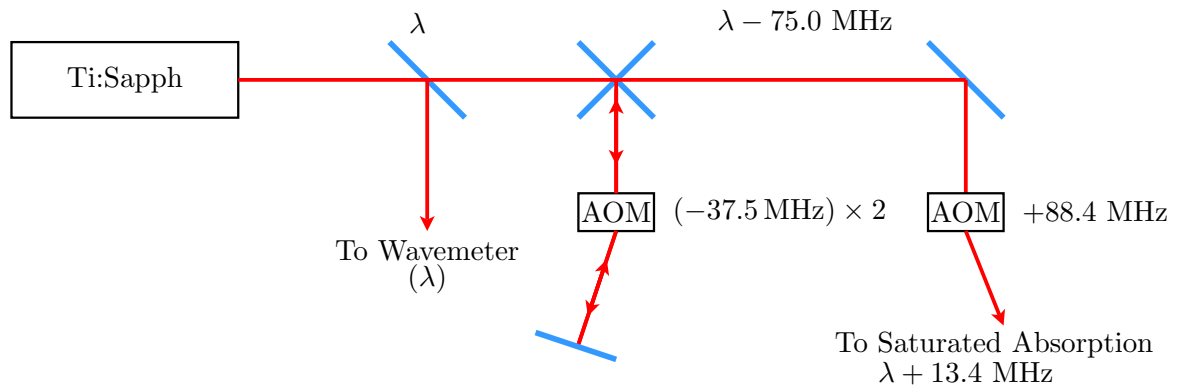


Figure A.1: AOM layout for the saturated absorption measurements.

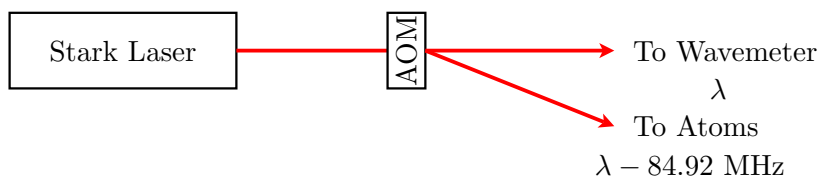


Figure A.2: AOM layout for the tune-out wavelength measurements.

Appendix B

Reduced Electric Dipole Matrix Elements

The electric dipole matrix elements $\langle \psi_0 | \mathbf{d} | \psi_f \rangle$ depend on the quantum numbers n , J , F , and m_F for both the initial and final states, as well as the polarization of the light. Following [38] we factor out the angular dependence of the dipole operator. Using the Wigner-Eckart Theorem, we rewrite the dipole matrix elements in terms of the Clebsch-Gordon coefficients and the reduced matrix elements

$$\langle F m_F | d_q | F' m'_F \rangle = \langle F || \mathbf{d} || F' \rangle \langle F m_F | F' m'_F; 1 q \rangle \quad (\text{B.1})$$

Eq. (B.1) can be written in terms of the Wigner 3- j symbol as

$$\langle F m_F | d_q | F' m'_F \rangle = \langle F || \mathbf{d} || F' \rangle (-1)^{F'+m_F-1} \begin{pmatrix} F' & 1 & F \\ m'_F & q & -m_F \end{pmatrix} \quad (\text{B.2})$$

	$q = -1$	$q = 0$	$q = +1$
$F' = 2$	$-\sqrt{\frac{1}{12}}$	$\sqrt{\frac{1}{6}}$	
$F' = 1$	$\frac{1}{2}$		

Table B.1: Dipole Matrix Elements for D_1 line transitions $F = 2, m_F = 2 \rightarrow F', m'_F = m_F + q$ expressed as multiples of $\langle J = 1/2 || \mathbf{d} || J' = 1/2 \rangle$

	$q = -1$	$q = 0$	$q = +1$
$F' = 3$	$\sqrt{\frac{1}{60}}$	$-\sqrt{\frac{1}{12}}$	$\frac{1}{2}$
$F' = 2$	$-\sqrt{\frac{1}{24}}$	$\sqrt{\frac{1}{12}}$	
$F' = 1$	$\sqrt{\frac{1}{40}}$		

Table B.2: Dipole Matrix Elements for D_2 line transitions $F = 2, m_F = 2 \rightarrow F', m'_F = m_F + q$ expressed as multiples of $\langle J = 1/2 || \mathbf{d} || J' = 3/2 \rangle$.

The F and F' dependence can be factored from the reduced matrix element in Eq. (B.2) to give

$$\langle F || \mathbf{d} || F' \rangle = \langle J || \mathbf{d} || J' \rangle (-1)^{F'+J+I+1} \sqrt{(2F'+1)(2F+1)} \begin{Bmatrix} J & J' & 1 \\ F' & F & I \end{Bmatrix} \quad (\text{B.3})$$

Where $\langle J || \mathbf{d} || J' \rangle$ is defined in terms of the resonant wavelength λ and lifetime Γ as

$$\langle J || \mathbf{d} || J' \rangle^2 = \frac{3}{2} (2J'+1) \left(\frac{\lambda}{2\pi} \right)^3 \epsilon_0 \hbar \Gamma \quad (\text{B.4})$$

For transitions in the D_1 line [38] $\langle J = 1/2 || \mathbf{d} || J' = 1/2 \rangle = 4.231(4)ea_0 = 3.588(4)10^{-29}$ C·m, while transitions in the D_2 line have $\langle J = 1/2 || \mathbf{d} || J' = 3/2 \rangle = 5.978(7)ea_0 = 5.069(6)10^{-29}$ C·m. Note, that Steck [38] defines the reduced dipole matrix element $\langle J || \mathbf{d} || J' \rangle_{\text{Steck}}$ as $\langle J || \mathbf{d} || J' \rangle_{\text{Steck}} = \frac{\langle J || \mathbf{d} || J' \rangle}{\sqrt{2J+1}}$.

Appendix C

Kinetic Imaging

C.1 Overview

The composite absorption images used in our analysis show the fraction of the probe light absorbed by the atoms. These images are created by dividing an image of the probe beam in the presence of the atoms, by an image of the probe beam without atoms. We refer to these images as the “atom” and “no atom” images, respectively.

Diffraction from dust and scratches as well as etaloning, result in an imaging beam which has a non-uniform intensity profile. The slight motion of optical surfaces as well as thermal effects cause shifts in the intensity profile. These shifts contribute to a noisy composite image.

Imaging noise of this type can be reduced by illuminating the atoms with a uniform intensity profile. However, such a profile is difficult to maintain in practice. A more robust method of reducing imaging noise can be achieved by reducing the time delay between the “atoms” and “no atoms” images. When using a standard readout method, the repetition rate of a camera is limited by the CCD readout time. In the lab we use a Pixis 1024 camera which is connected to a PC running WinView. The readout time of the full CCD on a Pixis 1024 camera is approximately 580 ms [39].

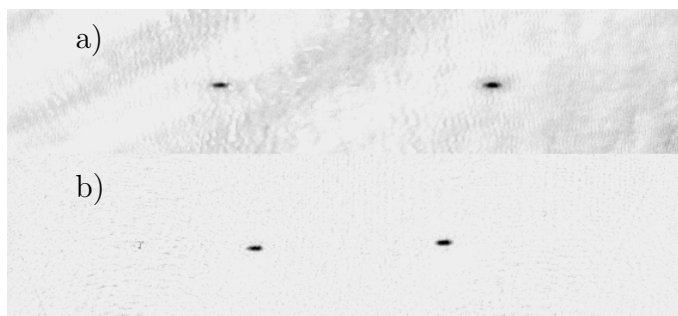


Figure C.1: a) An image formed using the normal readout method, where the “atoms” image is transferred to a computer before the “no atoms” image is taken. Changes in the probe beam’s profile, arising from slight shifts in diffraction patterns, result in a noisy, uneven, background. b) An image taken using kinetic imaging avoids background noise by significantly reducing the time delay between the “atoms” and “no atoms” images.

The time delay between two sequential images can be significantly reduced by postponing the image readout. This requires the camera to “hold” the first image while a second image is being acquired. In kinetics mode, this is achieved by exposing only the top portion of the CCD, then shifting the first image to the unused bottom portion of the CCD. To create a “blank” region in the CCD, suitable for storing an image, the bottom portion of the CCD must be optically masked. This is accomplished by positioning a razor blade in an image plane between the atoms and the CCD such that the shadow cast by the razor is imaged on to the bottom portion of the CCD. When using a camera in kinetics mode, the image repetition rate is limited by the time it takes to shift an image into the masked portion of the CCD. For the Pixis 1024 camera, it takes 1.6 ms to shift an image 512 lines down, into the masked region.

Once both images are acquired, the camera reads out a single composite image. The top and bottom halves of this image contain the first and second images, respectively. A home-built C++ code separates and divides the two images.

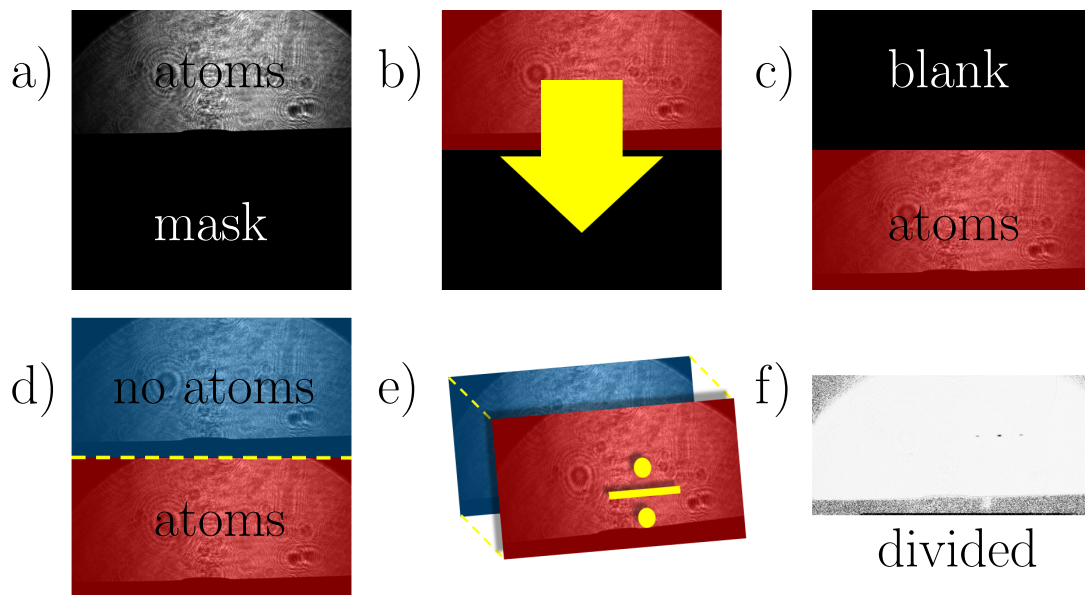


Figure C.2: Moving from left to right & from top to bottom: (a) An absorption image of the atoms is obtained in the top portion of the CCD, while a razor blade masks the bottom portion. (b) Charge that accumulated on the top portion of the CCD during “atoms” imaging is moved to the bottom half of the CCD. (c) This leaves the top portion of the CCD blank. (d) The top portion of the CCD is again exposed; creating an image of the “probe” beam in the absence of atoms. (e) The resulting image is transferred to a computer where a home-built C++ code splits and divides the two images. (f) The resulting divided image has little background noise.

C.2 Implementation

Our camera is set to kinetics readout mode using the WinView GUI, by navigating to **Setup > Hardware** and selecting the **Controller/Camera** tab. In this menu there are options to change the readout mode, vertical shift rate, and window size. The vertical shift rate describes the speed that an image is shifted into the masked region of the CCD, which, in turn, specifies the time delay between two sequential exposures. In our experiment, we chose the fastest vertical shift rate available: 3200 ns/row. In general, a camera may be used to take N sequential images using kinetics mode. The window size specifies the number of rows used for each exposure, which, in turn, specifies the number of sequential images taken. This occurs because, in kinetics mode, a camera continues to

acquire images until the CCD is unable to hold an additional image. When acquiring N images, the top $1/N$ portion of the CCD is used for image acquisition, while the bottom $(N-1)/N$ portion of the CCD is used for image storage. As usual, the bottom $(N-1)/N$ portion of the CCD must be masked. Thus, a camera with 1024 vertical lines may be used to capture two images with 512 vertical pixels, or three images with 341 vertical pixels. In general, a CCD with V vertical lines may be used to capture N sequential images in kinetics mode, by choosing a window size between $\lfloor \frac{V}{N-1} \rfloor + 1$ and $\lfloor \frac{V}{N} \rfloor$.

Because kinetics readout mode is designed for rapid image acquisition, the camera shutter is opened before the “trigger” pulse is received. As a result, the CCD is exposed to ambient light. To clear the charge that accumulates on the CCD, the camera must be set to “continuous cleaning” mode. This is accomplished using the WinView GUI by selecting **Experiment Setup** from the toolbar, navigating to the **Timing Mode** tab, and checking the **Continuous Cleans** box. In “continuous cleaning” mode, the camera delays the image exposure until the current cleaning cycle is complete. This introduces an unknown time delay between the “trigger” pulse and the actual image exposure. To limit the uncertainty in this time delay, we redefine the cleaning cycle, so that an image may be acquired after each strip of pixels is cleared. This is accomplished through the WinView GUI by navigating to the **Cleans/Skips** tab under the **Hardware Setup** menu and setting **Number of Cleans: 1** and **Number of Strips per Clean: 1**. For the Pixis 1024 camera, these settings result in a time delay bound by: $0 \mu s < \Delta t < 540 \mu s$. An important note regarding the “continuous cleans” time delay: although the time delay effects the timing of the CCD exposure, it in no way effects the timing of the absorption imaging pulse. Thus, for every experiment run, the image produced by the imaging pulse occurs at the same time relative to other aspects of the experiment.

Because the the “continuous cleaning” time delay varies with each experiment run, it may be difficult to time the absorption imaging pulses. The Logic Output on the Pixis 1024 camera provides a useful diagnostic for this problem. The Logic Output produces

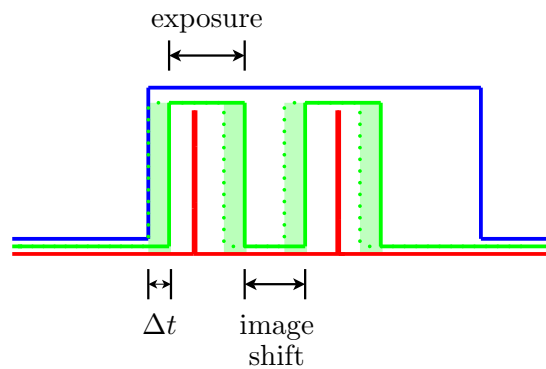


Figure C.3: The figure above shows the timing of the camera “trigger” in blue, alongside a digital signal controlling the imaging AOM in red. The green lines show the Shutter Logic Output of a Pixis 1024 camera. In Kinetic Mode, the Shutter Logic Output produces a high voltage when the CCD is acquiring an image. A time-delay Δt arises from the CCD “cleaning” cycle described in this section. The solid and dotted green lines represent the exposure times for the time-delay extrema, $\Delta t = 0 \mu\text{s}$ and $\Delta t = 540 \mu\text{s}$. The imaging AOM pulses must fall in the range of image exposure times common to all time-delays. A 1.6 ms delay between the two images occurs as the image from the top half of the CCD is transferred to the bottom half of the CCD.

a digital signal describing the internal state of the camera. The information carried by the Logic Output may be changed in WinView by navigating to the **Hardware Setup** menu and choosing the **Controller/Camera** tab. Selecting the Shutter Logic Output in kinetic mode tells the camera to produce a high voltage when the CCD is acquiring an image. In this mode the Logic Output produces a low voltage during the CCD cleaning cycle as well as during the image shift. When the cleaning cycle is finished the camera produces a high voltage for the duration of the exposure time, 2.0 ms in our experiment. The Logic output then produces a low voltage while the image is shifted under the masked portion of the CCD (1.6 ms), before switching back to a high voltage for the duration of the second exposure. For a successful imaging setup, the absorption imaging pulses must fall in the range of image acquisition times common to all time-delays. An image similar to the one shown in Figure C.3 may be obtained by connecting the camera “trigger”, the imaging AOM, and the Logic Output to an oscilloscope. The Logic Outputs for the full range of possible time-delays may be found by setting the display on the oscilloscope to

infinite persist, and then looping over the imaging routine.

C.3 Image Processing

Kinetic imaging produces a single composite image, with the top half containing the first image and bottom half containing the second. A home-built code uses the tiffio library to read and separate the two images. The code then generates and saves a divided image along with the separated Atom and No Atom images.

Image_Process.cpp

```

1  ///#include "stdafx.h" Breaks code; only use with MS VC compiler
2
3  #include <iostream>
4  #include <string>
5  #include <fstream>
6  #include <windows.h> // System command
7  #include <tiffio.h> // Read tiff files
8  #include <conio.h> // _getch (waits for key stroke)
9  #include <process.h> // multi-threading
10
11 using namespace std;
12
13 int SearchDirectory(string &LastFile ,
14                  uint32 &lowFileTime ,
15                  uint32 &highFileTime ,
16                  const std::string &refcstrRootDirectory ,
17                  const std::string &refcstrExtension);
18
19 int main(){
20     string NewestFile;
21     string DividedImage;
22     uint32 CompFileTimeLow;
23     uint32 CompFileTimeHigh;
24
25     // Find newest file with '.tif' extension
26
27     SearchDirectory( NewestFile , CompFileTimeLow , CompFileTimeHigh ,
28                    "c:\\datalocal\\today\\images\\PI" , "tif"  );
29
30     // Open newest kinetics mode picture
31
32     DividedImage = NewestFile;
33     DividedImage.replace(35,1,"d"); // Generate divided picture file name
34     TIFF* Ktif = TIFFOpen(NewestFile.c_str() , "r");
35
36     if (Ktif){

```

```

37     uint32 imagelength;
38     tsize_t scanline;
39     tdata_t Abuf, NAbuf;
40     uint32 row;
41     uint32 col;
42     uint16 Divbps, Divspp;
43     uint16 Abps, Aspp;
44     uint16 NAbps, NAspp;
45     uint16 bps, spp;
46     int nrows, ncolumns, orientation, planarconfig, photometric;
47 int i;
48
49 // Retrieve information from Tiff file header
50
51     TIFFGetField(Ktif, TIFFTAG_IMAGELENGTH, &imagelength);
52     TIFFGetField(Ktif, TIFFTAG_BITSPERSAMPLE, &bps);
53     TIFFGetField(Ktif, TIFFTAG_SAMPLESPERPIXEL, &spp);
54     TIFFGetField(Ktif, TIFFTAG_IMAGELENGTH, &nrows);
55     TIFFGetField(Ktif, TIFFTAG_IMAGEWIDTH, &ncolumns);
56     TIFFGetField(Ktif, TIFFTAG_ORIENTATION, &orientation);
57     TIFFGetField(Ktif, TIFFTAG_PHOTOMETRIC, &photometric);
58
59     planarconfig = 1;
60     scanline = TIFFScanlineSize(Ktif);
61     uint16 *AtomPixleValue;
62     uint16 *NoAtomPixleValue;
63     float *DividedPixleValue;
64
65 // Use information from Tiff file header to allocate memory for Atom, No
66 // Atom, and Divided Tiff files
67
68     DividedPixleValue = (float *) malloc(nrows*ncolumns*sizeof(float));
69     AtomPixleValue = (uint16 *) malloc(nrows*ncolumns*sizeof(uint16));
70     NoAtomPixleValue = (uint16 *) malloc(nrows*ncolumns*sizeof(uint16));
71
72 // Allocate memory for Tiff file scanlines (Tiff file is read one row at
73 // a time)
74
75     Abuf = (char*)_TIFFmalloc(scanline);
76     NAbuf = (char*)_TIFFmalloc(scanline);
77
78 // Loop through each row in Tiff file. Reads Atom image from top of
79 // Tiff image, and No Atom from bottom of the image.
80
81     for(i=0; i< (nrows/2); i++){
82         TIFFReadScanline(Ktif, Abuf, i); // Read row of Atoms image
83         TIFFReadScanline(Ktif, NAbuf, i+nrows/2); // Read row of No
84         // Atoms image
85         for (col = 0; col < ncolumns; col++){
86             DividedPixleValue[col+i*ncolumns] = float(((uint16 *)Abuf)[
87             col])/float((((uint16 *)NAbuf)[col]+1)); // Calculate divided image
88             AtomPixleValue[col+i*ncolumns] = (((uint16 *)Abuf)[col]);
89             NoAtomPixleValue[col+i*ncolumns] = (((uint16 *)NAbuf)[col])
90         };
91     };

```

```

85
86     }
87 }
88
89     _TIFFfree(Abuf);
90     _TIFFfree(NAbuf);
91     TIFFClose(Ktif);
92
93     // Write Divided Image Tiff file
94
95     TIFF *DividedOut= TIFFOpen(DividedImage.c_str(), "w");
96
97     // Set Tiff Tags (header values) for Divided Image
98
99     Divspp = 1; //normally there are 3 values per pixel for Red Green
100    Blue
101                //becuase the image is black and white there is only one
102    sample per pixel
103
104     Divbps = 32; //32 bits for float
105
106     TIFFSetField (DividedOut, TIFFTAG.IMAGEWIDTH, ncolumns); // set the
107    width of the image
108     TIFFSetField(DividedOut, TIFFTAG.IMAGELENGTH, (nrows/2)); // set
109    the height of the image
110     TIFFSetField(DividedOut, TIFFTAG.SAMPLESPERPIXEL, Divspp); // set
111    number of channels per pixel
112     TIFFSetField(DividedOut, TIFFTAG.BITSPERSAMPLE, Divbps); // set
113    the size of the channels
114     TIFFSetField(DividedOut, TIFFTAG.PLANARCONFIG, planarconfig);
115     TIFFSetField(DividedOut, TIFFTAG.PHOTOMETRIC, photometric);
116     TIFFSetField(DividedOut, TIFFTAG.SAMPLEFORMAT, 3); // 1 = uint16 3
117    = float
118
119     tsize_t Divlinebytes = Divspp * ncolumns; // length in memory of
120    one row of pixel in the image.
121
122     float *buf = NULL; // buffer used to store the row of pixel
123    information for writing to file
124
125     //Allocating memory to store the pixels of current row
126
127     if (TIFFScanlineSize(DividedOut) == Divlinebytes)
128         buf =(float *)_TIFFmalloc(Divlinebytes);
129     else
130         buf = (float *)_TIFFmalloc(TIFFScanlineSize(DividedOut));
131
132     // We set the strip size of the file to be size of one row of pixels
133     TIFFSetField(DividedOut, TIFFTAG.ROWSPERSTRIP, TIFFDefaultStripSize(
134    DividedOut, ncolumns*Divspp));
135
136     //Now writing image to the file one strip at a time
137
138     for (uint32 row = 0; row < (nrows/2); row++){

```

```

129         for (i=ncolumns-1; i>=0; i--){
130             ((float *)buf)[i] = DividedPixleValue[((nrows/2)-row-1)*
ncolumns+i];
131         }
132         if (TIFFWriteScanline(DividedOut, buf, row, 0) < 0)
133             break;
134     }
135     TIFFClose(DividedOut);
136
137     DividedImage.replace(35,1,"n");
138     TIFF *NoAtomOut= TIFFOpen(DividedImage.c_str(), "w");
139
140 // Set Tiff Tags for No Atoms
141
142     NAspp = 1; //normally there are 3 values per pixel for Red Green
Blue
143             //becuase the image is black and white there is only one
sample per pixel
144
145     NAbps = 16; //16 bits for uint16
146
147     TIFFSetField (NoAtomOut, TIFFTAG.IMAGEWIDTH, ncolumns); // set the
width of the image
148     TIFFSetField(NoAtomOut, TIFFTAG.IMAGELENGTH, (nrows/2)); // set
the height of the image
149     TIFFSetField(NoAtomOut, TIFFTAG.SAMPLESPERPIXEL, NAspp); // set
number of channels per pixel
150     TIFFSetField(NoAtomOut, TIFFTAG.BITSPERSAMPLE, NAbps); // set the
size of the channels
151     TIFFSetField(NoAtomOut, TIFFTAG.PLANARCONFIG, planarconfig);
152     TIFFSetField(NoAtomOut, TIFFTAG.PHOTOMETRIC, photometric);
153     TIFFSetField(NoAtomOut, TIFFTAG.SAMPLEFORMAT, 1); // 1 = uint16 3
= float
154
155     tsize_t NAlinebytes = NAspp * ncolumns; // length in memory of
one row of pixel in the image.
156
157     if (TIFFScanlineSize(NoAtomOut) == NAlinebytes)
158         buf = (float *)_TIFFmalloc(NAlinebytes);
159     else
160         buf = (float *)_TIFFmalloc(TIFFScanlineSize(NoAtomOut));
161
162     // We set the strip size of the file to be size of one row of pixels
163     TIFFSetField(NoAtomOut, TIFFTAG.ROWSPERSTRIP, TIFFDefaultStripSize(
NoAtomOut, ncolumns*NAspp));
164
165     //Now writing image to the file one strip at a time
166
167     for (uint32 row = 0; row < (nrows/2); row++){
168         for (i=ncolumns-1; i>=0; i--){
169             ((uint16 *)buf)[i] = NoAtomPixleValue[((nrows/2)-row-1)*
ncolumns+i];
170         }
171         if (TIFFWriteScanline(NoAtomOut, buf, row, 0) < 0)

```

```

172         break;
173     }
174
175     TIFFClose(NoAtomOut);
176
177     DividedImage.replace(35,1,"a");
178     TIFF *AtomOut= TIFFOpen(DividedImage.c_str(), "w");
179
180 // Set Tiff Tags for Atoms
181
182     Aspp = 1; //normally there are 3 values per pixel for Red Green Blue
183             //because the image is black and white there is only one
184             sample per pixel
185
186     Abps = 16; //16 bits for uint16
187
188     TIFFSetField (AtomOut, TIFFTAG.IMAGEWIDTH, ncolumns); // set the
189 width of the image
190     TIFFSetField (AtomOut, TIFFTAG.IMAGELENGTH, (nrows/2)); // set the
191 height of the image
192     TIFFSetField (AtomOut, TIFFTAG.SAMPLESPERPIXEL, Aspp); // set
193 number of channels per pixel
194     TIFFSetField (AtomOut, TIFFTAG.BITSPERSAMPLE, Abps); // set the
195 size of the channels
196     TIFFSetField (AtomOut, TIFFTAG.PLANARCONFIG, planarconfig);
197     TIFFSetField (AtomOut, TIFFTAG.PHOTOMETRIC, photometric);
198     TIFFSetField (AtomOut, TIFFTAG.SAMPLEFORMAT, 1); // 1 = uint16 3 =
199 float
200
201     tsize_t Alinebytes = Aspp * ncolumns; // length in memory of one
202     row of pixel in the image.
203
204     if (TIFFScanlineSize (AtomOut) == Alinebytes)
205         buf = (float *)_TIFFmalloc (Alinebytes);
206     else
207         buf = (float *)_TIFFmalloc (TIFFScanlineSize (AtomOut));
208
209     // We set the strip size of the file to be size of one row of pixels
210     TIFFSetField (AtomOut, TIFFTAG.ROWSPERSTRIP, TIFFDefaultStripSize (
211 AtomOut, ncolumns*Aspp));
212
213     //Now writing image to the file one strip at a time
214
215     for (uint32 row = 0; row < (nrows/2); row++){
216
217         for (i=ncolumns-1; i>=0; i--){
218             ((uint16 *)buf)[i] = AtomPixleValue [((nrows/2)-row-1)*
219 ncolumns+i];
220         }
221
222         if (TIFFWriteScanline (AtomOut, buf, row, 0) < 0)
223             break;
224     }
225     _TIFFfree (buf);
226

```

```

217         TIFFClose(AtomOut);
218     }
219 }
220
221 int SearchDirectory(string                &LastFile ,
222                   uint32                &lowFileTime ,
223                   uint32                &highFileTime ,
224                   const std::string     &refcstrRootDirectory ,
225                   const std::string     &refcstrExtension)
226 {
227
228 /* SearchDirectory returns the name and time stamp of the newest
229    file with a given file extension found in a specific directory.
230
231    Returns 1 if a file was found, 0 otherwise.
232
233    LastFile
234        Name of the newest file found
235
236    lowFileTime
237        Time stamp of newest file (low means it looks at smaller
238        time incerments [for example seconds])
239
240    highFileTime
241        Time stamp of newest file (high means it looks at larger
242        time incerments [for example days])
243
244    refcstrRootDirectory
245        Recursively searches for newest file in this directory
246
247    refcstrExtension
248        Look only for files ending with charaters matching this string
249 */
250
251     std::string    strFilePath;           // Filepath
252     std::string    strPattern;           // Pattern
253     std::string    strExtension;         // Extension
254     HANDLE         hFile;                // Handle to file
255     WIN32_FIND_DATA FileInformation;     // File information
256
257     FILETIME filetime;
258     uint32 minLowFileTime;
259     uint32 minHighFileTime;
260     string minFileTime;
261
262     minLowFileTime = 0;
263     minHighFileTime = 0;
264
265     strPattern = refcstrRootDirectory + "\\*.*";
266
267     // Search for files & folders in the specified directory
268     hFile = ::FindFirstFile(strPattern.c_str(), &FileInformation);
269
270     if ( hFile != INVALID_HANDLE_VALUE )

```

```

271 {
272     // Loop over all files
273     do
274     {
275         if ( FileInformation.cFileName[0] != '.' ){
276
277             // If a file is found record its path & filename
278             filetime = FileInformation.ftCreationTime;
279             strFilePath = refcstrRootDirectory + "\\\" + FileInformation.
cFileName;
280
281             // Check extension
282             strExtension = FileInformation.cFileName;
283             strExtension = strExtension.substr(strExtension.rfind("k.") + 2);
284
285             if ( strExtension == refcstrExtension ){
286
287                 // If the extension matches test the time stamp
288                 filetime = FileInformation.ftCreationTime;
289
290                 // First test high time
291                 if ( filetime.dwHighDateTime > minHighFileTime){
292                     minHighFileTime = filetime.dwHighDateTime; // Record
newest file time stamp
293                     minLowFileTime = filetime.dwLowDateTime;
294                     minFilePath = strFilePath; // Record newest file name
295                 }
296                 // If high times equal check low times
297                 else if ( filetime.dwHighDateTime == minHighFileTime ) {
298
299                     if ( filetime.dwLowDateTime > minLowFileTime){
300                         minLowFileTime = filetime.dwLowDateTime;
301                         minFilePath = strFilePath;
302                     }
303
304                 }
305             }
306         }
307     } while ( ::FindNextFile(hFile, &FileInformation) == TRUE );
308
309     // Record name & time stamp of newest file
310     LastFile = minFilePath;
311     highFileTime = minHighFileTime;
312     lowFileTime = minLowFileTime;
313
314     // Close handle
315     ::FindClose(hFile);
316
317     DWORD dwError = ::GetLastError();
318     if ( dwError != ERROR_NO_MORE_FILES )
319         return dwError;
320 }
321 return 0;
322 }

```

Bibliography

- [1] J. D. Jackson. *Classical Electrodynamics*. John Wiley and Sons, Inc., third edition edition (1999).
- [2] V. S. Letokhov. “Doppler line narrowing in a standing light wave.” *JETP Lett.* **7**, 272 (1968).
- [3] J. D. Miller, R. A. Cline, and D. J. Heinzen. “Far-off-resonance optical trapping of atoms.” *Phys. Rev. A* **47**, R4567 (1993).
- [4] R. Cambi, D. Cappelletti, G. Liuti, and F. Pirani. “Generalized correlations in terms of polarizability for van der waals interaction potential parameter calculations.” *J. Chem. Phys.* **95**, 1852 (1991).
- [5] E. A. Power and T. Thirunamachandran. “Casimir-polder potential as an interaction between induced dipoles.” *Phys. Rev. A* **48**, 4761 (1993).
- [6] J. Mitroy, M. S. Safronova, and C. W. Clark. “Theory and applications of atomic and ionic polarizabilities.” *J. Phys. B: At. Mol. Opt. Phys.* **43**, 202001 (2010).
- [7] V. A. Dzuba, V. V. Flambaum, and O. P. Sushkov. “Polarizabilities and parity non-conservation in the cs atom and limits on the deviation from the standard electroweak model.” *Phys. Rev. A* **56** (1997).

-
- [8] A. A. Vasilyev, I. M. Savukov, M. S. Safronova, and H. Berry. “Measurement of the 6s-7p transition probabilities in atomic cesium and a revised value for the weak charge q_w .” *Phys. Rev. A* **66** (2002).
- [9] M. S. Safronova, S. G. Porsev, U. I. Safronova, M. G. Kozlov, and C. C. W. “Blackbody-radiation shift in the sr optical atomic clock.” *Phys. Rev. A* **87** (2013).
- [10] A. D. Ludlow and et al. “Sr lattice clock at 1×10^{16} fractional uncertainty by remote optical evaluation with a ca clock.” *Science* **319** (2008).
- [11] L. Hollberg and J. L. Hall. “Measurement of the shift of rydberg energy levels induced by blackbody radiation.” *Phys. Rev. Lett.* **53** (1984).
- [12] T. F. Gallagher and W. E. Cooke. “Interactions of blackbody radiation with atoms.” *Phys. Rev. Lett.* **42** (1979).
- [13] B. Deissler. *Measuring Polarizabilities Using a Bose-Einstein Condensate Interferometer*. Ph.D. thesis, University of Virginia (2008).
- [14] K. D. Bonin and M. A. Kadar-Kallen. “Theory of the light-force technique for measuring polarizabilities.” *Phys. Rev. A* **47**, 944 (1993).
- [15] L. J. LeBlanc and J. H. Thywissen. “Species-specific optical lattices.” *Phys. Rev. A* **75**, 053612 (2007).
- [16] B. Arora, M. S. Safronova, and C. W. Clark. “Tune-out wavelengths of alkali-metal atoms and their applications.” *Phys. Rev. A* **84**, 043401 (2011).
- [17] P. F. Griffin. *Laser Cooling and Loading of Rb into A Large Period, Quasi-Electrostatic, Optical Lattice*. Ph.D. thesis, Durham University (2005).
- [18] R. Shankar. *Principles of Quantum Mechanics*. Plenum Press, second edition edition (1994).

-
- [19] A. Derevianko and S. G. Porsev. “Accurate evaluation of parameters of lattice clocks.” (2007). Retrieved August 15, 2016, from http://wolfweb.unr.edu/homepage/andrei/WWW-tap/Publications/optClockBook_Chapter_11_
- [20] Y. B. Zel’dovich. “The quasienergy of a quantum-mechanical system subject to a periodic action.” *Sov. Phys. JETP* **24**, 1006 (1967).
- [21] V. Kapoor and D. Bauer. “Floquet analysis of real-time wavefunctions without solving the floquet equation.” (2012). 1110.1518v2.
- [22] B. K. Sahoo and B. Arora. “Magic wavelengths for trapping the alkali-metal atoms with circularly polarized light.” *Phys. Rev. A* **87**, 023402 (2013).
- [23] N. L. Manakov, V. D. Ovsiannikov, and L. E. Rapoport. “Atoms in a laser field.” *Phys. Rep.* **141**, 319 (1986).
- [24] F. L. Kien, P. Schneeweiss, and A. Rauschenbeutel. “Dynamical polarizability of atoms in arbitrary light fields: General theory and application to cesium.” *Eur. Phys. J. D* **67**, 92 (2013).
- [25] M. J. Morrison, V. A. Dzuba, and A. Derevianko. “Possibility of stark-insensitive cotrapping of two atomic species in optical lattices.” *Phys. Rev. A* **83**, 013604 (2011).
- [26] J. M. Reeves. *An Atom Waveguide For Interferometry With A Bose-Einstein Condensate of ^{87}Rb* . Ph.D. thesis, University of Virginia (2006).
- [27] C. S. Adams and E. Riis. “Laser cooling and trapping of neutral atoms.” *Prog. Quant. Electr.* **21**, 1 (1997).
- [28] K. J. Hughes, B. Deissler, J. H. T. Burke, and S. C. A. “High-fidelity manipulation of a bose-einstein condensate using an optical standing wave.” *Phys. Rev. A* **76**, 035601 (2007).

-
- [29] Y. J. Wang, D. Z. Anderson, V. M. Bright, E. A. Cornell, Q. Diot, T. Kishimoto, M. Prentiss, R. A. Saravanan, S. R. Segal, and S. Wu. “Atom michelson interferometer on a chip using a bose-einstein condensate.” *Phys. Rev. Lett.* **94**, 090405 (2005).
- [30] O. Garcia, B. Deissler, K. J. Hughes, J. M. Reeves, and C. A. Sackett. “Bose-einstein-condensate interferometer with macroscopic arm separation.” *Phys. Rev. A* **74**, 031601(R) (2006).
- [31] M. S. Safronova and U. I. Safronova. “Critically evaluated theoretical energies, lifetimes, hyperfine constants, and multipole polarizabilities in ^{85}rb .” *Phys. Rev. A* **83**, 052508 (2011).
- [32] C. D. Herold, V. D. Vaidya, X. Li, S. L. Rolston, and J. V. Porto. “Precision measurement of transition matrix elements via light shift cancellation.” *Phys. Rev. Lett.* **109**, 243003 (2012).
- [33] M. S. Safronova and W. R. Johnson. “All-order methods for relativistic atomic structure calculations.” *Adv. At. Mol., Opt. Phys.* **55**, 191 (2008).
- [34] U. Volz and S. H. “Precision lifetime measurements on alkali atoms and on helium by beam-gas-laser spectroscopy.” *Physica Scripta* **T65**, 48 (1996).
- [35] R. H. Leonard, A. J. Fallon, C. A. Sackett, and M. S. Safronova. “High precision measurement of the ^{87}rb d-line tune-out wavelength.” *Adv. At. Mol., Opt. Phys.* **55**, 191 (2008).
- [36] R. F. Gutterres, C. Amiot, A. Fioretti, C. Gabbanini, M. Mazzoni, and O. Dulieu. “Determination of the ^{87}rb 5p state dipole matrix element and radiative lifetime from the photoassociation spectroscopy of the $\text{Rb}_2 0_g(p_{3/2})$ long-range state.” *Phys. Rev. A* **66**, 024502 (2002).
- [37] J. E. Simsarian, L. A. Orozco, G. D. Sprouse, and W. Z. Zhao. “Lifetime measurements of the 7p levels of atomic francium.” *Phys. Rev. A* **57**, 2448 (1998).

-
- [38] D. A. Steck. “Rubidium 87 d line data, revisoun 1.6.” Retrieved May 31, 2015, from <http://steck.us/alkalidata/rubidium87numbers.1.6.pdf>.
- [39] Princeton Instruments Imaging Group. *Pixis: 1024 eXcelon Rev. N3*.